A numerical study of water exchange in sill fjords and the effect of coastal climate change

Master of Science Thesis in Applied and Computational Mathematics

Vilde Margrethe Sætre Strand

Department of Mathematics
University of Bergen

April 2019

Acknowlegements

First of all, I would like to thank my supervisor Jarle Berntsen for his generous support, guidance and useful feedbacks. Thank you for introducing me to the interesting world of ocean modeling, and for your enthusiasm and patient.

Many thanks to Trond Einar Isaksen at Norwegian Research Centre (NORCE) for providing hydrographic data used in this study, and to Dag L. Aksnes for providing his unpublished paper.

Finally, I want to thank my family and friends. Lunches and tea breaks with fellow students at the Department of Mathematics and friends outside the University has made this experience so much better. I am so grateful to my grandparents for being the best role models, and to my parents for their love and encouragement.

Vilde Margrethe,
April 2019

Abstract

The dynamics of basin water exchange in sill fjords are governed by external factors. This thesis addresses how climate change on the coast may affect the water exchange of the basin water. A three-dimensional hydrostatic ocean model, the Bergen Ocean Model (BOM), is applied to simulate inflows from the coast into an idealized fjord topography, resembling Sørfjorden, located outside Bergen, Norway. Consecutive events of inflow of water from the coast are simulated, and two main cases of water exchange are investigated, with and without coastal warming. In the case of coastal warming, 1°C and 2°C of warming are investigated.

The lower 100 meters of the basin water is marked. With no coastal warming 88 % of this marked bottom water is replaced by ambient water, after two coastal inflows. For the cases with 1°C and 2°C of coastal warming, only 15 % and 3% are replaced. The model results indicate that a coastal warming of 1°C has a major effect on the water exchange of the lower basin water. A 2°C warming results in a further decrease of the basin exchange. Less frequent events of basin water exchange may cause deoxygenation in the basin water due to e.g. biological consumption, and hence worse water quality. A worsening of the water quality due to climate change will potentially have significant consequences for the fjord ecosystems and services, e.g. aquacultures.

Contents

Chapter 1

Introduction: Water exchange in sill fjords

The Norwegian coast consists of several long and deep fjords. These areas provide the enviroment for important aquaculture industries (Sætre, 2007). Fjords are sheltered from harsh weather and ocean waves, which is an important benefit for these industries.

At the entrance of many fjords there is a sill, separating the fjord from the ocean. These fjords are called sill fjords, and the fjord area below the sill level is referred to as the fjord basin. The water quality in such fjords is dependent on several factors, one of the essential factors being the exchange of water between the fjord and coastal waters. Exchange of the basin water occurs when coastal water above the sill level is denser than the water in the basin, resulting in a partial or complete water exchange of the basin water. Due to the sill, the water exchange between the fjord and the coast in sill fjords is limited. The upper part is typically often exchanged, while exchange of the lower basin water is dependent on coastal water over the sill level being denser than the lower basin water. Consequently, events of total basin water exchange may not happen for several years (Soltveit and Jensen, 2018). Few events of exchange may result in poor water quality and low oxygen levels in

the basin water. In stagnation periods, i.e. periods with no exchange of the basin water, dissolved oxygen in the basin water is steadily consumed due to biological consumption, resulting in poor water quality. Pollution from fish farming in the fjords may also contribute to a worsening of the water quality (Soltveit and Jensen, 2018). Due to the sill, poor oxygen levels in the basin is a typical characteristic of many sill fjords with deep basins. In order to maintain good water quality in sill fjords, regular exchange of the basin water is crucial.

Over the last four decades, the oxygen level near the bottom of various deep fjord basins has declined (Johansen et al., 2018; Aksnes et al., 2019). During the same time period, there has been an increasing trend in the temperature of the coastal water (Bakketeig et al., 2017). Observations show a significant temperature increase in the North Atlantic Water along the coast, especially after 1990. This is the oceanic source water for many of the fjords at the Norwegian coast (Sætre, 2007). During the last four decades, it is assumed that the temperature of the North Atlantic Water has increased approximately 1°C (Bakketeig et al., 2017). The temperature of the coastal water varies from year to year, due to natural variations, but parts of this temperature increase seem to be connected to global warming (Bakketeig et al., 2017). Results from a previous study indicate that the observed deoxygenation in the fjord basins is a result of this coastal warming (Aksnes et al., 2019). They suggest that warmer coastal water leads to less frequent water exchange, thus deoxygenation of the basin water.

In the present study, a three-dimensional hydrostatic ocean model, the Bergen Ocean Model (BOM), is applied to mimic events of coastal inflow into a sill fjord. The objective of the study is to investigate the effect of coastal warming on the exchange of the basin water. An idealized fjord topography, resembling Sørfjorden, located outside Bergen, is used as the model area.

Motivation and Outline

The primary goal of this thesis is to investigate how warming of the coastal water may affect the basin exchange in a sill fjord. A further worsening of the water quality due to climate change will potentially have significant consequences for the fjord ecosystems and services, e.g. aquacultures. New insight on water exchange in fjordic systems will contribute to a sustainable management of coastal and fjord areas.

The thesis is divided into the following chapters:

In Chapter 2 the governing equations for geophysical flow are presented. The equations are hard to solve, and by introducing the Boussinesq approximation, Reynolds averaging and scale analysis, some of the equations are simplified. The turbulent closure problem is briefly introduced, and boundary conditions are stated.

In Chapter 3 the three-dimensional σ-coordinate ocean model, the Bergen Ocean Model (BOM), is introduced. The model is based on solving the governing equations, described in Chapter 2, and will be used to run numerical simulations in this thesis.

In Chapter 4 the model setup for the problem is described. The model area, initial values, boundary conditions, and the Froude number are defined. Finally, an overview of the numerical simulations done in this thesis is given.

In Chapter 5 results from the numerical simulations is presented and discussed. There will be one case with only tidal force present, which will be called the base case. In the two main cases coastal inflows are added; coastal water with and without warming.

In Chapter 6 a summary and conclusions are given, together with remarks on further work.

An overview of the symbols used is provided in the Appendix.

Chapter 2

The Governing Equations for Geophysical Flow

2.1 Geophysical Flow

Geophysical flow describes the dynamics in the ocean and the atmosphere. The dynamics in the ocean will be the focus of this thesis. The main features that distinguish geophysical flows from other areas of fluid dynamics are the effects due to the rotation of the earth, and vertical stratification, as geophysical flows typically involve fluids of different densities (Kundu et al., 2016). Typically, the length scales (L) of the motions in geophysical flow are larger than the height scales (H) (Cushman-Roisin and Beckers, 2011). Therefore, horizonal velocity components (U, V) are generally much bigger than vertical velocity component (W), i.e.

$$U, V \gg W \ . \tag{2.1}$$

Accordingly, for simplification, the horizontal and vertical velocity components are split up. We define $\mathbf{U} = (U, V)$ [m s^{-1}] as the horizontal velocity components in the x- and y-direction, respectively, when using Cartesian co-

ordinates. The vertical velocity component in the z-direction is denoted W [m s^{-1}].

The governing equations for geophysical flow in the ocean are introduced in the following section. This chapter is mainly based on (Berntsen, 2004) and (Cushman-Roisin and Beckers, 2011).

2.2 The Governing Equations

The Continuity Equation

The general form of the continuity equation can be expressed

$$\frac{\partial \rho}{\partial t} + \nabla \cdot (\rho \mathbf{U}) + \frac{\partial}{\partial z}(\rho W) = 0 \ , \tag{2.2}$$

where ρ is the density [kg m^{-3}] of the fluid, t [s] is the time. The two-dimensional nabla operator ∇ is defined as $(\frac{\partial}{\partial x}, \frac{\partial}{\partial y})$, and the x-, y- and z-axes are directed eastward, northward and upward, respectively. Using the definition of the material derivative;

$$\frac{\mathrm{D}\rho}{\mathrm{D}t} \equiv \frac{\partial \rho}{\partial t} + \mathbf{U} \cdot \nabla \rho + W \frac{\partial \rho}{\partial z} \ ,$$

we obtain

$$\frac{1}{\rho}\frac{\mathrm{D}\rho}{\mathrm{D}t} + \nabla \cdot \mathbf{U} + \frac{\partial W}{\partial z} = 0 \ . \tag{2.3}$$

In flows that can be assumed incompressible, like the ocean, the change in ρ is very small in comparison to ρ itself, so the first term in (2.3) becomes very small compared to the second term. Thus, for incompressible flow, equation (2.2) is simplified to

$$\nabla \cdot \mathbf{U} + \frac{\partial W}{\partial z} = 0 \ . \tag{2.4}$$

When assuming incompressible flow, the continuity equation (2.4) express conservation of volume.

The Momentum Equations

The Navier-Stokes equations describe the motion of fluids. The equations arise when applying Newtons second law to fluid motion, and are, written on vector form, given by

$$\frac{\partial \mathbf{U_{3D}}}{\partial t} + \mathbf{U_{3D}} \cdot \nabla \mathbf{U_{3D}} + 2\boldsymbol{\Omega} \times \mathbf{U_{3D}} = -\frac{1}{\rho}\nabla p + \mathbf{g} + \frac{\mu}{\rho}\nabla^2 \mathbf{U_{3D}} \ . \qquad (2.5)$$

To write the equation on vector form, the three-dimensional velocity vector, $\mathbf{U_{3D}} = (U, V, W)$ [m s^{-1}], is used. Henceforth, the horizontal and vertical velocities are split up, as stated in Section 2.1. The two first terms on the left-hand side are the material derivative of $\mathbf{U_{3D}}$, describing the rate of change of $\mathbf{U_{3D}}$ moving with the fluid. When studying fluid on a rotating planet, we need to take into account the rotation of the Earth. By introducing the Coriolis acceleration, $2\boldsymbol{\Omega} \times \mathbf{U_{3D}}$, the force due to Earths rotation are included. Here, the angular velocity vector of the Earth is defined as $\boldsymbol{\Omega} = (0, \Omega\cos\phi, \Omega\sin\phi)$, where Ω [rad s^{-1}] is the rotation rate of the Earth, and ϕ [rad] is defined as the position on the surface of the Earth in the north-south direction. On the right hand side of equation (2.5) we have the pressure gradient ∇p, gravitational acceleration $\mathbf{g}$, and the viscosity term $\frac{\mu}{\rho}\nabla^2 \mathbf{U}_{3D}$, where μ [kg m^{-1} s^{-1}] is the viscosity of the fluid. The viscosity is a measure of the fluid's ability to resist deformation due to shear stress. The ratio $\frac{\mu}{\rho}$ is called the molecular viscosity, denoted $\nu = \frac{\mu}{\rho}$ [m^2 s^{-1}].

Computing the cross product in the Coriolis term results in

$$2\boldsymbol{\Omega} \times \mathbf{U_{3D}} = 2\Omega\big[W\cos\phi - V\sin\phi, U\sin\phi, -U\cos\phi\big] \ .$$

The expression can be simplified using equation (2.1),

$$2\boldsymbol{\Omega}\times\mathbf{U_{3D}} \approx \big[-2\Omega V\sin\phi, 2\Omega U\sin\phi, -2\Omega U\cos\phi\big] = \big[-fV, fU, -2\Omega U\cos\phi\big] \ ,$$

where $f = 2\Omega\sin\phi \approx 10^{-4}$ rad s^{-1} is called the Coriolis parameter. This simplification is only valid away from the equator ($\phi = 0$). The z-component

of the Coriolis parameter is often neglected because $H \ll L$, so we only have contributions in the x- and y-direction. Using the Cartesian coordinates system with x and y as horizontal coordinates, and z as the vertical coordinate, the components of equation (2.5) are

$$\frac{\partial U}{\partial t} + \mathbf{U} \cdot \nabla U + W\frac{\partial U}{\partial z} - fV = -\frac{1}{\rho}\frac{\partial p}{\partial x} + \frac{\mu}{\rho}\nabla^2 U \ , \tag{2.6}$$

$$\frac{\partial V}{\partial t} + \mathbf{U} \cdot \nabla V + W\frac{\partial V}{\partial z} + fU = -\frac{1}{\rho}\frac{\partial p}{\partial y} + \frac{\mu}{\rho}\nabla^2 V \ , \tag{2.7}$$

$$\frac{\partial W}{\partial t} + \mathbf{U} \cdot \nabla W + W\frac{\partial W}{\partial z} = -\frac{1}{\rho}\frac{\partial p}{\partial z} + g + \frac{\mu}{\rho}\nabla^2 W \ . \tag{2.8}$$

We now apply the Boussinesq approximation, Reynolds averaging and scale analysis to simplify the equations (2.6)-(2.8).

In the ocean, there are small density variations (Cushman-Roisin and Beckers, 2011). The density can be expressed $\rho = \rho_0 + \rho'(x, y, z, t)$ with $|\rho'| << \rho_0$, where ρ_0 is the mean density, and ρ' is the variation around the mean. The Boussinesq approximation states that due to small density variations, we can neglect ρ' in all terms except where multiplied with the gravitational acceleration g.

By using the property for geophysical flow (2.1), and doing a scale analysis (Cushman-Roisin and Beckers, 2011), some of the small terms in the z-component, equation (2.8), can also be neglected. We then end up with the hydrostatic balance, equation (2.11). The hydrostatic balance states that the pressure given at a specific depth is equal to the weight of the fluid above. Thus, the weight of the fluid balance the pressure.

When looking at a turbulent flow, we are most often interested in finding the momentum equation for the mean state. To obtain this averaged momentum equations, Reynolds decomposition is applied. Reynolds decomposition refers to the process of decomposing the variables into two parts; a mean and a fluctuation (Haidvogel and Beckmann, 1999). Thus, a variable u is

decomposed into $u = \overline{u} + u'$, where $\overline{u}$ is the mean, and u' the fluctation from the mean. This is done for the velocities (U, V, W), the pressure (p) and the density (ρ). By using properties of averaging, the Reynolds averaged momentum equations are obtained (Kundu et al., 2016). Since we will only be working with the averaged momentum equation for the rest of this thesis, we from now on replace $\overline{u}$ with u for all the variables. The components of the Reynolds averaged momentum equations are

$$\frac{\partial U}{\partial t} + \mathbf{U} \cdot \nabla U + W\frac{\partial U}{\partial z} - fV = -\frac{1}{\rho_0}\frac{\partial p}{\partial x} + \frac{\partial}{\partial z}(K_M \frac{\partial U}{\partial z}) + F_x \ , \tag{2.9}$$

$$\frac{\partial V}{\partial t} + \mathbf{U} \cdot \nabla V + W\frac{\partial V}{\partial z} + fU = -\frac{1}{\rho_0}\frac{\partial p}{\partial y} + \frac{\partial}{\partial z}(K_M \frac{\partial V}{\partial z}) + F_y \ , \tag{2.10}$$

$$\rho g = -\frac{\partial p}{\partial z} \ . \tag{2.11}$$

The molecular viscosity, $\nu = \frac{\mu}{\rho}$, has been replaced with the vertical eddy viscosity, K_M, and the horizontal viscosity terms F_x and F_y. These terms will be further discussed when the Turbulent Closure Problem is introduced later in Chapter 2.3. The terms F_x and F_y are defined

$$F_{x,y} = \frac{\partial}{\partial x}(A_M \frac{\partial (U,V)}{\partial x}) + \frac{\partial}{\partial y}(A_M \frac{\partial (U,V)}{\partial y}) \ , \tag{2.12}$$

where the horizontal viscosity, A_M, are computed as proposed by Smagorinsky (1963), or set constant. The momentum equations, (2.9)-(2.11), express conservation of momentum. Notice that the z-component (2.11) is the hydrostatic balance.

To obtain an expression for the pressure (p) at the depth z, the vertical component of the momentum equation (2.11) is integrated from z to the surface elevation η,

$$p = \int_z^\eta \rho g dz = \rho_0 g\eta + g\int_z^0 \rho(\acute{z})d\acute{z}. \tag{2.13}$$

The first term on the right hand side of (2.13) is pressure due to surface elevation, while the second is the internal pressure. Pressure due to the motion of the fluid, called non-hydrostatic pressure, is neglected.

The Conservation Equations

The conservation equation for temperature (T) and salinity (S) is given by

$$\frac{\partial \Gamma}{\partial t} + \mathbf{U} \cdot \nabla \Gamma + W \frac{\partial \Gamma}{\partial z} = \frac{\partial}{\partial z}(K_H \frac{\partial \Gamma}{\partial z}) + F_\Gamma \ , \tag{2.14}$$

where Γ is the temperature or the salinity. Equation (2.14) is also used to describe conservation of *passive tracers* fields; θ (marking of the bottom water), ξ (marking of the coastal water) and O_2 (marking of the oxygen). These passive tracers will be introduced in Chapter 4. The temperature and salinity are related to the density through the equation of state (2.16), they influence the dynamics in the flow, and are called *active tracers*. The passive tracers have no effect on the flow, they passively drift in the flow.

In the conservation equation (2.14), K_H is the vertical eddy diffusivity, which will be further discussed in section 2.3. The horizontal diffusivity term F_Γ is defined by

$$F_\Gamma = \frac{\partial}{\partial x}(A_H \frac{\partial \Gamma}{\partial x}) + \frac{\partial}{\partial y}(A_H \frac{\partial \Gamma}{\partial y}) \ , \tag{2.15}$$

where the horizontal eddy diffusivity A_H are computed as proposed by Smagorinsky (1963), or set constant.

The Equation of State

The equation of state relate the salinity and temperature to the density,

$$\rho = \rho(T, S) \ . \tag{2.16}$$

In this thesis the simplified equation of state suggested by Wang (1984) is used, which gives a nonlinear dependence of density on temperature and salinity.

2.3 The Turbulent Closure Problem

When solving the governing equations for a model area, a grid must be introduced, which represents the points where the equations will be solved. The grid used in the present study is introduced in Chapter 4. The nonlinearity of the Navier-Stokes equations (2.5) creates a flow of energy from large scale motion towards scales that can not be represented in a finite grid size. Motions occurring on smaller scales than the grid cells are not represented in the model (figure 2.1). These unresolved motions on subgrid scale may affect resolved motions on larger resolvable scales and the effects of subgrid scale motions are therefore important to include in the model. This can be viewed as *the turbulent closure problem*. To address this problem, eddy viscosity and diffusivity terms are introduced in order to parameterize the unresolved motions on subgrid scale.

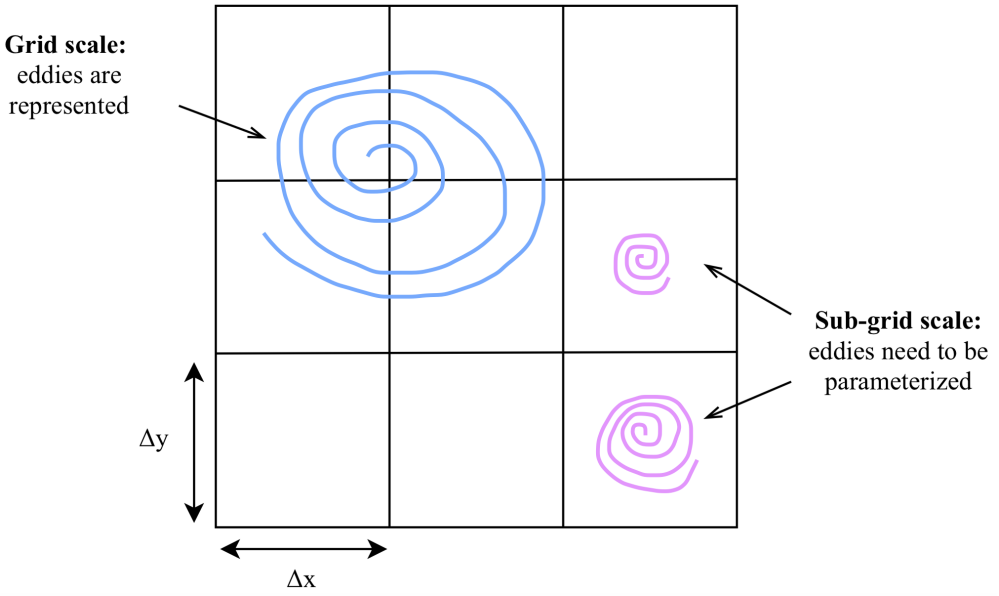

Figure 2.1: An illustration of a grid with resolved and unresolved eddies. The resolved eddies (blue) are represented in the model, while the unresolved (purple) needs to be parameterized.

To close the system of equations given in Chapter 2.2 we need equations for the eddy viscosity and diffusivity terms. The horizontal grid size is often bigger than the vertical grid size, consequently covering a larger amount of unresolved motion (Cushman-Roisin and Beckers, 2011). Accordingly, two different terms are needed; one horizontal and one vertical.

Horizontally, the system is closed by introducing the horizontal eddy viscosity (A_M) and diffusivity (A_H), in equation (2.12) and (2.15). A_M and A_H are set constant or computed as proposed by Smagorinsky (1963).

For vertical closure, equations for the vertical viscosity (K_M) and diffusivity (K_H) are needed. They can be set constant, or be calculated by simple models, but this is often not sufficient (Berntsen, 2004). In model areas where tidal forcing and stratification are important, Berntsen (2004) recommends using the turbulence closure model suggested by Mellor and Yamada (1982). In the present study, the Mellor-Yamada turbulence scheme (Mellor and Yamada, 1982) is used to compute K_M and K_H.

The characteristic length and velocity scales for the turbulent kinetic energy ($q^2/2$) are defined as l and q, respectively. The length scale l is often called the turbulence macro scale (Hanert et al., 2006). The governing equations for turbulent kinetic energy ($q^2/2$), and turbulent macro scale (l) are given by

$$\begin{aligned}\frac{\partial q^2}{\partial t} + \mathbf{U}\cdot\nabla q^2 + W\frac{\partial q^2}{\partial z} &= \frac{\partial}{\partial z}(K_q\frac{\partial q^2}{\partial z})+ \\ 2K_M\left[\left(\frac{\partial U}{\partial z}\right)^2+\left(\frac{\partial V}{\partial z}\right)^2\right] + \frac{2g}{\rho_0}K_H\frac{\partial \rho}{\partial z} - \frac{2q^3}{B_1 l}&,\end{aligned} \tag{2.17}$$

$$\begin{aligned}\frac{\partial q^2 l}{\partial t} + \mathbf{U}\cdot\nabla q^2 l + W\frac{\partial q^2 l}{\partial z} &= \frac{\partial}{\partial z}(K_q\frac{\partial q^2 l}{\partial z})+ \\ lE_1K_M\left[\left(\frac{\partial U}{\partial z}\right)^2+\left(\frac{\partial V}{\partial z}\right)^2\right] + \frac{lE_1 g}{\rho_0}K_H\frac{\partial \rho}{\partial z} - \frac{q^3}{B_1}\tilde{W}&,\end{aligned} \tag{2.18}$$

where

$$\tilde{W} = 1 + E_2 \left(\frac{l}{\kappa L} \right)^2 \tag{2.19}$$

and

$$L^{-1} = (\eta - z)^{-1} + (H + z)^{-1}. \tag{2.20}$$

Here, $\kappa = 0.4$ is the von Karman constant.

The problem is closed by computing the vertical viscosity and diffusivity according to

$$K_M = qlS_M \ , \tag{2.21}$$

$$K_H = qlS_H \ , \tag{2.22}$$

and the diffusivity of the turbulence model equations K_q by

$$K_q \ = \ 0.20lq \ . \tag{2.23}$$

S_M and S_H are stability functions which are derived analytically (Hanert et al., 2006). Defining G_H by

$$G_H = \frac{l^2}{q^2} \frac{g}{\rho_0} \frac{\partial \rho}{\partial z} \ , \tag{2.24}$$

and the empirical values

$$(A_1, A_2, B_1, B_2, C_1, E_1, E_2) = (0.92, 0.74, 16.6, 10.1, 0.08, 1.8, 1.33) \ ,$$

S_M and S_H are given by

$$S_H[1 - (3A_2B_2 + 18A_1A_2)G_H] = A_2[1 - 6A_1/B_1] \ , \tag{2.25}$$

and

$$S_M[1 - 9A_1A_2G_H] - S_H[18A_1^2 + 9A_1A_2)A_1[1 - 3C_1 - 6A_1/B_1] \ . \tag{2.26}$$

The Richardson Number

The second term on the right hand side of equations (2.17) and (2.18), contain the shear velocities, while the third terms contain the vertical density gradient. Investigating these terms can give an important indication of how turbulent the flow is (Cushman-Roisin and Beckers, 2011). The Richardson number (Ri) is defined as the ratio between the vertical density gradient and the velocity shear:

$$Ri = -\frac{g}{\rho_0} \frac{\frac{\partial \rho}{\partial z}}{(\frac{\partial U}{\partial z} + \frac{\partial V}{\partial z})^2} \ . \tag{2.27}$$

This dimensionless number express the importance of stratification effects in the flow, and how turbulent it is. A Richardson number of order much less than unity, $Ri \ll 1$, signify that the stratification effects are negligible and the flow is receptive to mixing and turbulence. For $Ri \gg 1$, the stratification effects are dominant, and the flow is less receptive to turbulence. Thus, a dominant vertical density gradient signify a stable flow with limited turbulence and mixing. Larger shear velocities result in more turbulence.

The *critical* Richardson number (Ri_c) indicates when the flow changes from a stable to an unstable regime. When $Ri < Ri_c$, the flow is turbulent and unstable. The turbulent kinetic energy and length scale produced in the Mellor-Yamada turbulence scheme also grows for small values of Ri ($Ri << Ri_c$). The Richardson number will be used when discussing the results of the numerical experiments in Chapter 5.

2.4 Boundary Conditions

In Chapter 2.2 the governing equations were introduced. To specify their solution, some conditions at the boundaries of the model area need to be stated.

Kinematic Boundary Conditions

The kinematic boundary condition states that there can be no fluid flow through solid boundaries, only tangential to it. Thus, fluid velocity normal to a solid boundary must be zero.

On the side walls, we apply the free slip condition for the flow. We also need no flow through the side walls, i.e.

$$U_n = 0, \tag{2.28}$$

where U_n is the component of the velocity that is normal to the wall.

At the free surface, $z = \eta(x, y)$, no fluid particles can cross the boundary. Thus, a particle on the boundary will always remain on the boundary. The vertical velocities at the free surface and the bottom, $z = -H(x, y)$, must therefore satisfy

$$W_0 = \frac{\partial \eta}{\partial t} + U\frac{\partial \eta}{\partial x} + V\frac{\partial \eta}{\partial y}, \tag{2.29}$$

$$W_b = -U_b\frac{\partial H}{\partial x} - V_b\frac{\partial H}{\partial y}. \tag{2.30}$$

Here, $\mathbf{U_b} = (U_b, V_b)$ are the horizontal velocities near the bottom. Equation (2.30) states that the vertical velocity must be tangent to the bottom boundary, and that there can be no mass flux though the boundary. At the free surface, we need to take into account that the boundary is moving with the fluid, so (2.29) gain an extra term.

Dynamic Boundary Conditions

The dynamic boundary condition states that stress across the free surface must be continuous.

At the free surface, $z = \eta(x, y)$, the flow must satisfy

$$\rho_0 K_M \left(\frac{\partial U}{\partial z}, \frac{\partial V}{\partial z} \right) = (\tau_{0x}, \tau_{0y}), \tag{2.31}$$

$$\rho_0 K_H \left(\frac{\partial T}{\partial z}, \frac{\partial S}{\partial z} \right) = (\dot{T}_0, \dot{S}_0), \tag{2.32}$$

where $\tau_{\mathbf{0}} = (\tau_{0x}, \tau_{0y})$ is the surface wind stress, $\dot{T}_0$ is the heat flux at the surface, and $\dot{S}_0$ is the rainfall and evaporation at the surface.

At the bottom, the bottom drag will have an effect on the horizontal velocities given by

$$\rho_0 K_M \left(\frac{\partial U}{\partial z}, \frac{\partial V}{\partial z} \right) = (\tau_{bx}, \tau_{by}) \ . \tag{2.33}$$

The bottom stress, $\tau_{\mathbf{b}} = (\tau_{bx}, \tau_{by})$, may be expressed as

$$\tau_{\mathbf{b}} = \rho_0 C_D |\mathbf{U}_b| \mathbf{U}_b \ , \tag{2.34}$$

where $\mathbf{U}_b$ is the velocity vector in the grid cell closest to the bottom. The drag coefficient C_D is specified by

$$C_D = \max[0.0025, \frac{\kappa^2}{(ln(z_b/z_0))^2}] \ . \tag{2.35}$$

Here, z_0 is the bottom roughness parameter set to 0.01 meters, z_b is the distance from the nearest grid point to the bottom, and $\kappa = 0.4$ is the Von Karman constant.

Chapter 3

The Bergen Ocean Model

Numerical ocean modeling is based on solving the governing equations introduced in Chapter 2. The ocean model used for the simulations in this thesis is the Bergen Ocean Model (BOM). BOM is a hydrostatic, σ-coordinate numerical ocean model developed by Berntsen *et al.* (2004). In BOM the equations are discretized by finite difference method on an staggered Arakawa C-grid (Arakawa, 1966). For a further description of the Arakawa C-grid and the model, see Berntsen (2004).

The σ-coordinate System

Due to variations in depth and bottom topography in the ocean, models using Cartesian z-coordinate in the vertical direction have troubles resolving areas near the bottom. Introducing a terrain-following coordinate system will give a smoother representation of the bottom topography.

In BOM, the governing equations are converted into a σ-coordinate system, see figure 3.1. This is a terrain following coordinate system where the variables (x, y, z, t) are transformed to (x^*, y^*, σ, t^*), where

$$x^* = x \quad y^* = y \quad \sigma = \frac{z - \eta}{H + \eta} \quad t^* = t. \tag{3.1}$$

Here, (x, y, z) are Cartesian coordinates, t [s] is time, H [m] is the depth $z = H(x, y)$, and η [m] is the surface displacement from $z = 0$. H is the undisturbed depth, hence $H + \eta$ is the total depth. In contrast to the z-coordinate system, the number of vertical levels in the σ-coordinate system are equal for all regions in the domain, and the thickness of the layers are not uniform. σ increase from $\sigma = 0$ at the surface ($z = \eta$) to $\sigma = -1$ at the bottom ($z = -H(x, y)$).

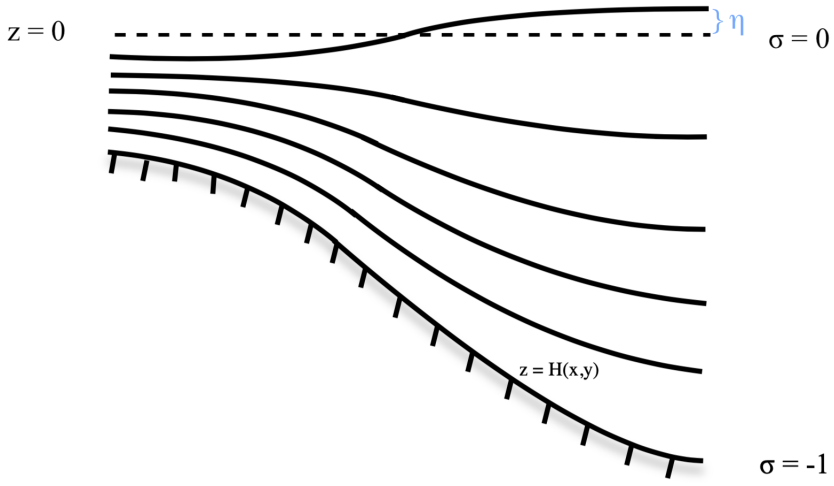

Figure 3.1: An illustration of the σ-coordinate system. The surface displacement from $z = 0$ is defined as η, and σ increase from $\sigma = 0$ at the surface, $z = \eta$, to $\sigma = -1$ at the bottom, $z = -H(x, y)$.

Chapter 4

Setup for Sørfjorden

Sørfjorden is a sill fjord located between Osterøy, outside Bergen, and the mainland. The fjord is 425 meters at the deepest, see figure 4.1. Sørfjorden consists of several sills with associated basins, and in this thesis, we will focus on one of these.

In the present study, an idealized topography of the fjord is used as model area. The model area consists of a rectangular fjord basin with a sill which separates the basin from the outer part of the fjord, leading to the coast. The center of the sill is situated 10 kilometers into the model area. The depth of the fjord basin is idealized to be 400 meters and the sill at 200 meters depth. The fjord area is set to be 1.5 kilometers wide in the y-direction and 35.5 kilometers long in the x-direction, including boundaries. A two-dimensional illustration of the model area is shown in figure 4.2.

The grid consists of 142×8 cells horizontally with equidistant grid sizes $\Delta x = 250$ meters and $\Delta y = 250$ meters. There are 60 σ-layers vertically. The vertical resolution is 6.67 meter at 400 meters depth and is chosen based on a resolution analysis done by Sand (2018). The center of a grid cell is denoted as (i, j, k). Here, (i, j, k) are the positions in the x-, y-, and z-direction, respectively.

For the rest of this thesis, the z-axis in the figures are labeled as *depth*, and the x-axis as *length*, of the fjord. Two-dimensional plots of the model area, like figure 4.2, are vertical planes through the center in the y-direction. The model area outside the sill, leading to the coast, will be referred to a the *outer part* of the fjord, and the part inside the sill as the *inner part* of the fjord. Likewise, the part of the sill facing the coast will be referred to as the *outer part* of the sill, and the part facing the fjord basin as the *inner part* of the sill.

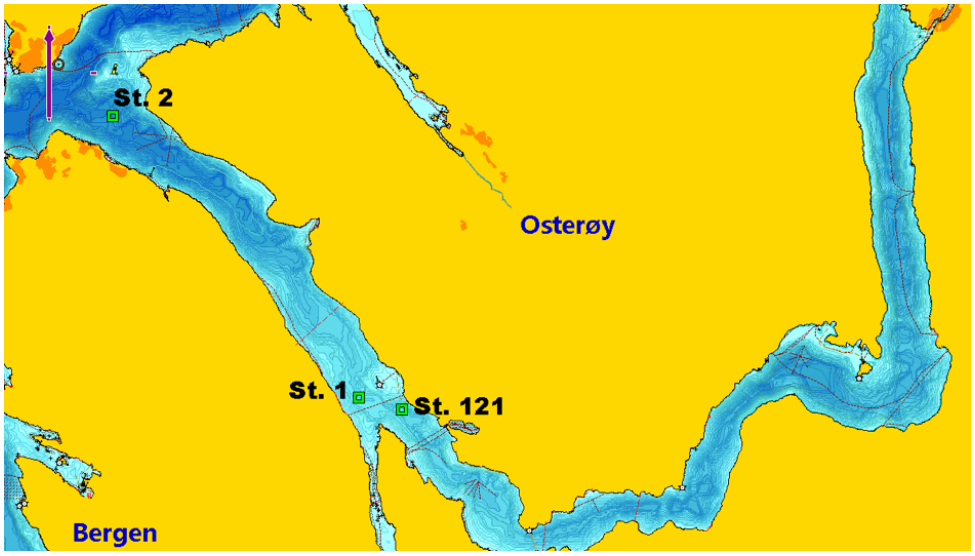

Figure 4.1: Map of Sørfjorden, located outside Bergen. The three stations where NORCE has collected hydrographic data is marked in the figure. Courtesy of Einar Bye-Ingebrigtsen, NORCE.

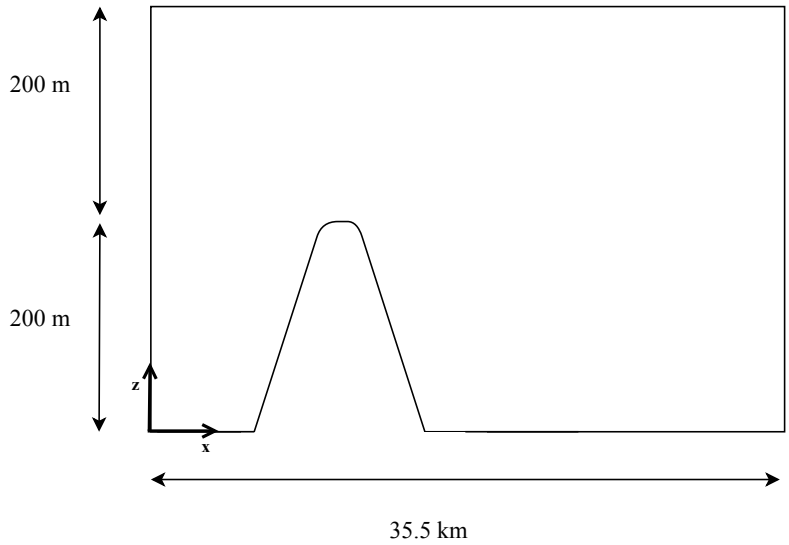

Figure 4.2: A two-dimensional illustration of the model area. The fjord area is set to be 35.5 kilometers long in the x-direction and 1.5 kilometers wide in the y-direction (into the paper). The depth of the fjord is idealized to be at 400 meters, and the sill at 200 meters of depth.

4.1 Initial Values

Initially, there is no flow, $U = V = W = 0$ ms^{-1}, and the surface elevation η is zero, $\eta = 0$ meter. The Coriolis force, due to the rotation of the Earth, is important in fjords wider than the baroclinic Rossby radius of deformation, which is typically 2-5 kilometers in Norwegian fjords (Sætre, 2007). Sørfjorden is less than 2 kilometers at its widest, so the Coriolis parameter f is set to zero.

4.1.1 Initial Values of the Active Tracers

The active tracers, temperature and salinity, are related to the density through the equation of state (2.16); thus they actively influence the dynamics in the flow. The initial temperature and salinity field in the fjord model are assumed to be horizontally homogeneous. The profiles are based on hydrographic data from Norwegian Research Centre (NORCE), measured at three different stations in Sørfjorden as shown in figure 4.1. The data were collected at different locations and seasonal times, and has therefore been averaged in time and space. Defining the temperature or salinity at a specific depth as γ, the profiles are calculated from the observations (γ_{obs}) at each specific depth and time, according to

$$\gamma(z) = \frac{1}{n} \sum_{\forall x,y,t} \gamma_{obs}(x, y, z, t) \ . \tag{4.1}$$

Here, n is the number of observations at each depth. The profiles are made stable by ensuring that the data for temperature is decreasing with depth, and salinity increasing with depth. It is checked that this gives a stable initial density profile, i.e. $\frac{\partial \rho}{\partial z} \leq 0$ (figure 4.3). The data is then interpolated to the depths in the model, and the salinity and temperature profiles are smoothed vertically using a Shapiro filter (Shapiro, 1975). Defining $\gamma_{i,j,k}$ as the temperature/salinity at the center of the grid cell (i, j, k), the vertically Shapiro filtering on γ one time is given by

$$\widetilde{\gamma_{i,j,k}} = \frac{1}{4}(\gamma_{i,j,k-1} + 2\gamma_{i,j,k} + \gamma_{i,j,k+1}) \ , \tag{4.2}$$

where $\widetilde{\gamma}$ is the filtered value of the temperature/salinity. The density profile is computed from the salinity and temperature profiles by the equation of state (2.16), given in Chapter 2.2. The profiles are plotted in figure 4.3 and 4.4.

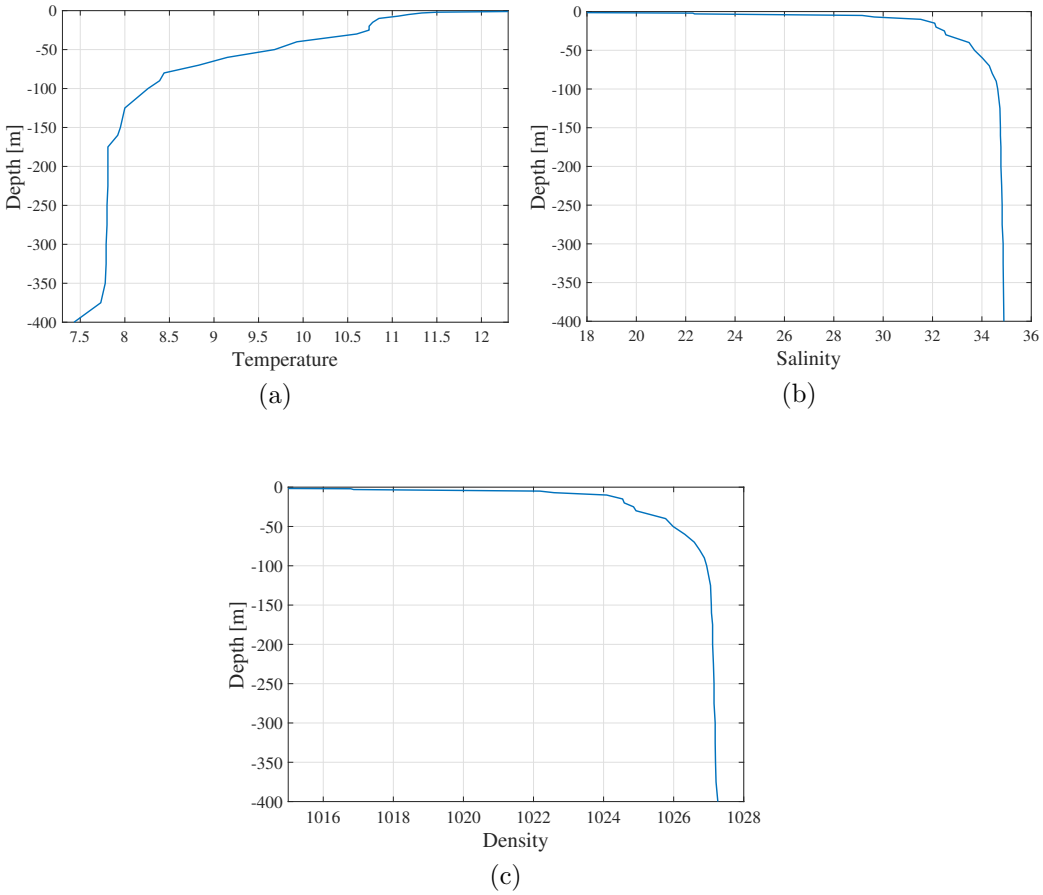

Figure 4.3: The initial profiles of (a) temperature T [°C], (b) salinity S [psu], and (c) density ρ [kg m^{-3}] of the fjord water. The profiles are based on hydrographic data from NORCE, and are assumed to be horizontally homogeneous.

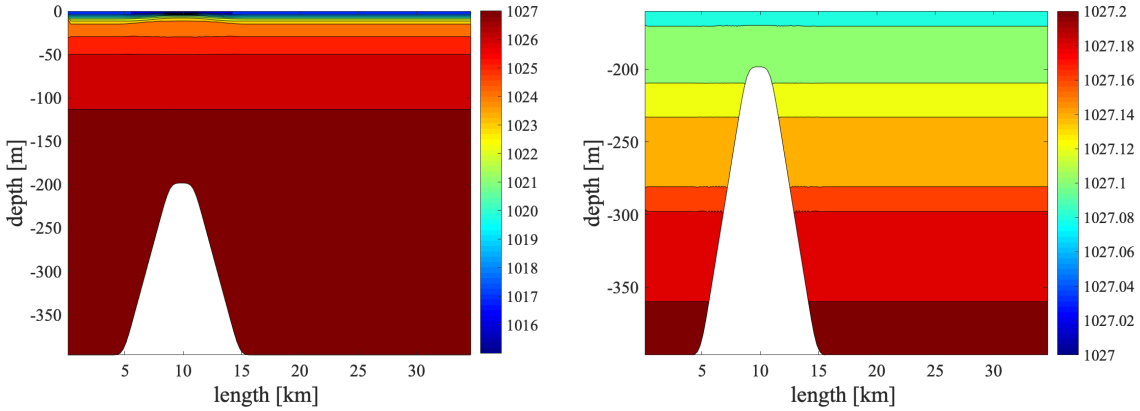

Figure 4.4: The initial profile of density, ρ [kg m^{-3}], of the fjord water. Figure (a) shows the entire depth of the model area, while only the lower 160 meters are plotted in (b).

4.1.2 Initial Values of the Passive Tracers

In order to track properties, three passive tracers are added to the model; the oxygen (O_2), bottom water (θ), and coastal water (ξ). These passive tracers do not influence the dynamics in the flow, but drift passively in the flow.

Marking of the Oxygen

Initially, there are two profiles for the oxygen in the model area; one outside, and one inside the sill. The oxygen profiles are assumed to be horizontally homogeneous and are based on data from NORCE, measured evenly throughout 2016 and 2017, of the water in the inner and outer part of Sørfjorden. The profiles are smoothed vertically with a Shapiro filter (Shapiro, 1975), similar to equation (4.2). A oxygen concentration below 2 ml l^{-1} is often considered as hypoxic, i.e. the oxygen concentration is so low that it can no

longer support most aquatic life (Zhang et al., 2015). Figure 4.5 shows the initial oxygen profiles.

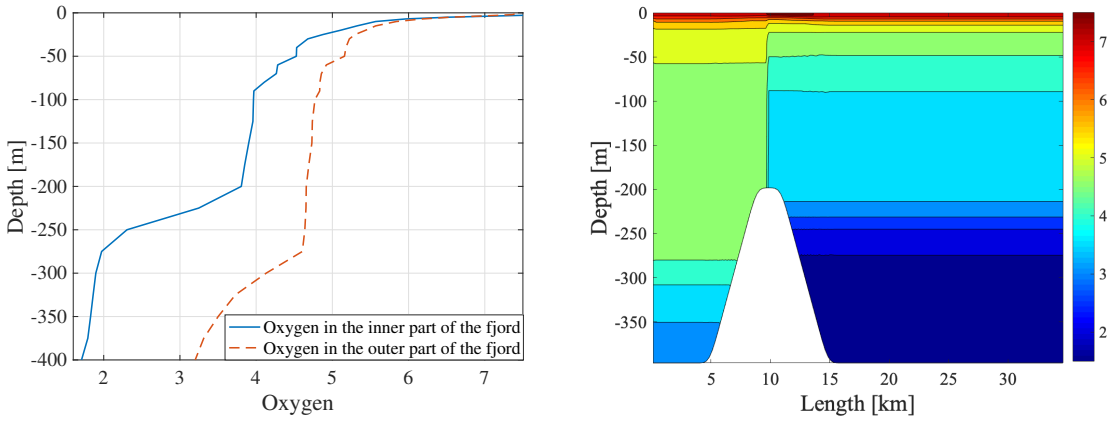

(a) (b)

Figure 4.5: The initial profile of oxygen, O_2 [ml l^{-1}], presented in (a) a graph, and (b) a contour plot. The inner and outer profiles overlaps above the sill and are assumed to be horizontally homogeneous.

Marking of the Bottom Water

The most oxygen-depleted water is typically found in the lower basin water. To investigate the residence time of this water a tracer, $\theta(x, y, z, t)$, is added to the model. The tracer is marking the water initially situated in the lower 100 meters of the basin water, referred to as the *marked bottom water*, and is used to study how the marked bottom water evolves over time. Initially, all the cells in the lower 100 meters of the basin is marked 1.0, and everywhere else 0.0 (figure 4.6a). Thus, the initial profile for the tracer is

$$\theta(x, y, z, 0) = \begin{cases} 0.0, & \text{if outside the sill.} \\ 0.0, & \text{if } -300 \text{ m} < z < 0 \text{ m and inside the sill.} \\ 1.0, & \text{if } -400 \text{ m} < z \leq -300 \text{ m and inside the sill.} \end{cases} \tag{4.3}$$

where

$$\text{outside the sill} \Leftrightarrow 0 \text{ km} < x < 10 \text{ km},$$

$$\text{inside the sill} \Leftrightarrow 10 \text{ km} \leq x < 35 \text{ km}.$$

Marking of the Coastal Water

To investigate the evolution of the coastal water in the fjord model a passive tracer, $\xi(x, y, z, t)$, is added to the model for marking the coastal water. Initially, there is no coastal water in the model area, hence the initial profile for the ξ-tracer is set to

$$\xi(x, y, z, 0) = 0.0 \qquad \forall\ x, y, z. \tag{4.4}$$

A contour plot of the initial profile is shown in figure 4.6b.

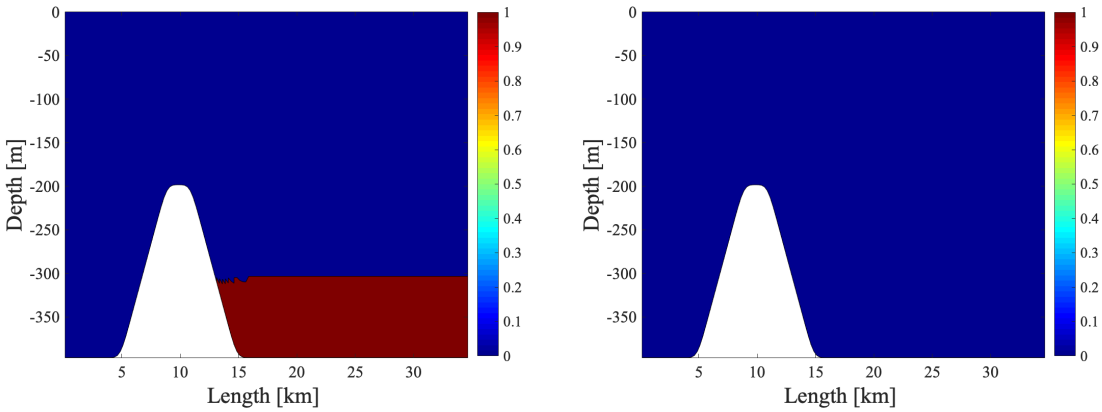

Figure 4.6: The initial profile of the passive tracers (a) $\theta(x, y, z, 0)$, marking the bottom water, and (b) $\xi(x, y, z, 0)$, marking the coastal water. Initially, there is no coastal water in the model area. The disturbance by the sill in (a) is a result of an interpolation error done by MATLAB when plotting.

4.2 Boundary Conditions

At the lateral boundaries to the north, south, and east, and at the bottom of the model area, there is land. Therefore, these boundaries are closed. There can be no volume flux through these boundaries. The surface wind stress $\tau_{\mathbf{0}} = (\tau_{0x}, \tau_{0y}) = 0$, the heat flux at the surface $\dot{T}_0 = 0$ and the rainfall and evaporation at the surface $\dot{S}_0 = 0$.

To the west, there is an open boundary. This is the mouth of the fjord, where inflows of water from the coast arise. The flow relaxation scheme (FRS) is used to achieve a realistic interaction with the coast outside the boundary.

4.2.1 The Flow Relaxation Scheme

At the open boundary in the west, the flow relaxation scheme (FRS), suggested by Martinsen and Engedahl (1987), is applied as an open boundary condition. Within a specified relaxation zone at the boundary, called the FRS-zone, the variable ϕ is being updated according to

$$\phi \;=\; (1 - \alpha(x))\phi_M + \alpha(x)\phi_F \;. \tag{4.5}$$

Here, ϕ_M is the unrelaxed model-value of the variable, ϕ_F is the forced value, and $\alpha \in [\,0, 1\,]$ is the relaxation parameter in the FRS-zone. An illustration of the FRS-zone is given in figure 4.7. The relaxation parameter decreases uniformly from $\alpha = 1$ at the outer part of the FRS-zone, to $\alpha = 0$ in the inner part towards the interior model domain.

In this study, the FRS-zone is 10 grid-cells wide, equivalent to 2.5 km, and the variables T, S, O_2, ξ, and θ are relaxed towards a forced solution throughout the FRS-zone. The forced values of the variables is set equal to the initial values at the boundary.

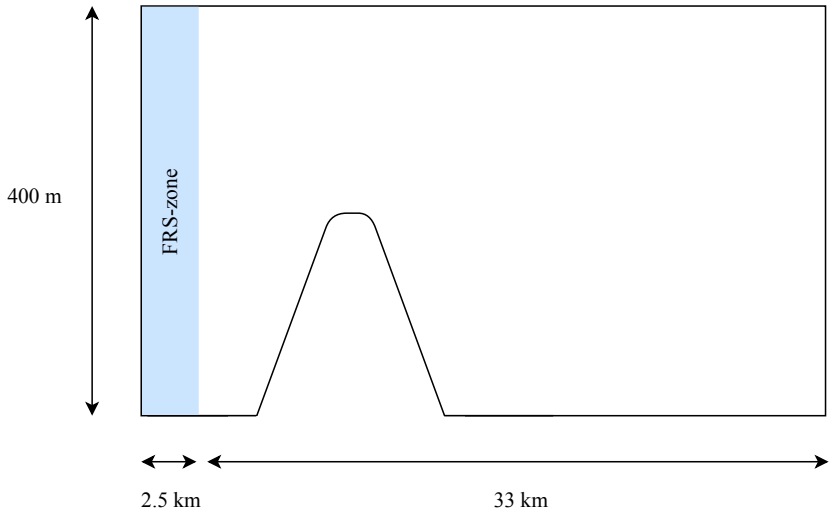

Figure 4.7: Illustration of the FRS-zone in the model area.

4.2.2 External Forcing - Tide and Coastal Water

Tidal forcing and inflows of coastal water are added to the model as external forces.

The Tide

The tide is caused by gravitational forces from the moon and the sun, resulting in a rise and fall of the sea level. This force generates a wave, moving the water masses in the fjord back and forth. Using FRS, the tidal motion is simulated by imposing the main component of the tide, called M_2, at the open boundary in the west. The period of M_2 is $T_{M_2} = 12.12$ hours.

The Density Profile of The Coastal Water

The oceanic source water for the basin water in Sørfjorden is the North Atlantic Water, flowing along the Norwegian coast. This source water is

also found at the coastal hydrographic station Ytre Utsira (Institute of Marine Research, 2018). Thus, for the purpose of this thesis, a reasonable approximation of the coastal water profile is obtained by using the temperature and salinity profile at Ytre Utsira.

The mean temperature, averaged over depth and season, at Ytre Utsira in 1978 was 7.3°C. In 2018 the mean temperature was measured to be 8.6°C, hence the difference in average temperature during the last 40 years is 1.3°C. For the purpose of the present study, a coastal temperature of 7°C, 8°C and 9°C, will correspond to no coastal warming, 1°C of coastal warming and 2°C of coastal warming, respectively.

Mainly salinity controls the density of the coastal water, not the temperature. For simplicity, the temperature is set constant. The density gradient is small at depths and the exchange of water may therefore still be affected by changes in the temperature. By choosing

$$T_{coast}(z) = 7.00\ ^\circ\text{C} \qquad \forall\ z\ , \tag{4.6}$$

$$S_{coast}(z) = S_{max} - \Delta S \cdot e^{-\tau z} \qquad \forall\ z\ , \tag{4.7}$$

a reasonable profile for the coastal water, representing no coastal warming, is obtained. We set $S_{max} = 35.1$ psu, $\Delta S = 3.0$ psu and the constant $\tau = -\frac{1}{60}\ \text{m}^{-1}$. These values and the exponential expression for the salinity are chosen based on typical values for the salinity at Ytre Utsira, and so that some coastal water above the sill level is dense enough to exchange the bottom water in the fjord basin. The density profile of the coastal water, corresponding to no coastal warming, is computed by the equation of state (2.16), and are plotted together with the profile of the fjord in figure 4.8. Notice that the coastal water at 142 meters and below is denser than the water in the fjord at the bottom; $\rho_{coast,142m} > \rho_{fjord,400m}$. Consequently, when coastal water moves over the sill some will be dense enough to intrude into the bottom of the fjord basin.

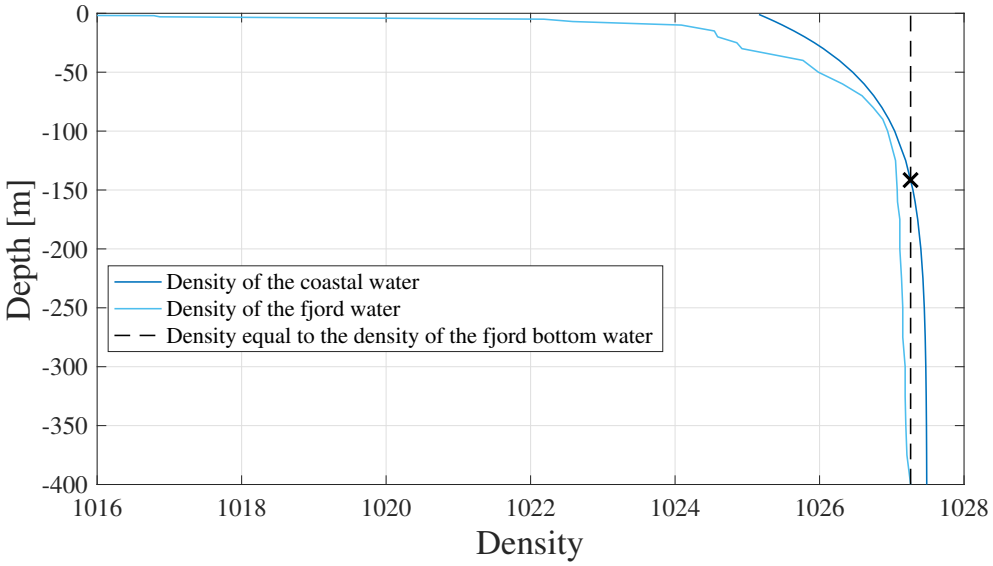

Figure 4.8: The density profile of the fjord and coastal water. The profile of the coastal water represents a situation of no coastal warming. Coastal water with density equal to the density of fjord water at bottom of the fjord is marked "x". The sill is at 200 meters depth.

Hence, the coastal temperature of 7°C represents a situation of successfull (partial or complete) water exchange with no coastal warming. To investigate how this water exchange is effected by warming of the coastal water, a coastal temperature of 8°C and 9°C will also be investigated during the numerical simulations described in Chapter 4.6.

Applying FRS to Mimic Events of Coastal Inflow

Inflow of water from the coast into the fjords often happends during long periods of northerly wind at the coast (Johansen et al., 2018). Wind from the north, produce coastal upwelling along the coast, and may generate internal Kelvin waves where the coast line is broken by a fjord mouth (Asplin et al., 1999; Cushman-Roisin and Beckers, 2011). The internal waves, propagating

into the fjord, cause events with inflow of coastal water. We want to use an open boundary condition that mimics consecutive events with inflow of dense water from the coast toward the open boundary of the model area. The salinity in the FRS zone is updated according to

$$S_{FRS}(z,t) = (1-\beta(t))S_F(z) + \beta(t)S_C(z) \ , \tag{4.8}$$

where $S_F(z)$ is the salinity of the fjord water, $S_C(z)$ is the salinity of the coastal water, and $\beta(t) \in [\,0,1\,]$ is the relaxation parameter. To obtain n consecutive events with inflow from the coast, a time-dependent function for β is introduced,

$$\beta(t) = \begin{cases} 0 & \text{for } t < t_0,\ t > t_0 + nT_p, \\ a(\frac{1}{2} - \frac{1}{2}\cos\omega(t-t_0)) & \text{else.} \end{cases} \tag{4.9}$$

Here, $a \in [\,0,1\,]$ is the dimensionless amplitude, ω [s^{-1}] the frequency, t [s] the time and $T_p = \frac{2\pi}{\omega}$ [s] the period. During this thesis, the period will be specified in hours, for practical reasons. The starting time for the inflow is defined as t_0 [s]. The relaxation paramteter is plotted in figure 4.9. A maximum inflow of coastal water and $a = 1$ means that there is only coastal water in the FRS-zone, and $a = 0$ means no coastal water in the zone. By varying the amplitude a, the amount of inflow from the coast can be adjusted.

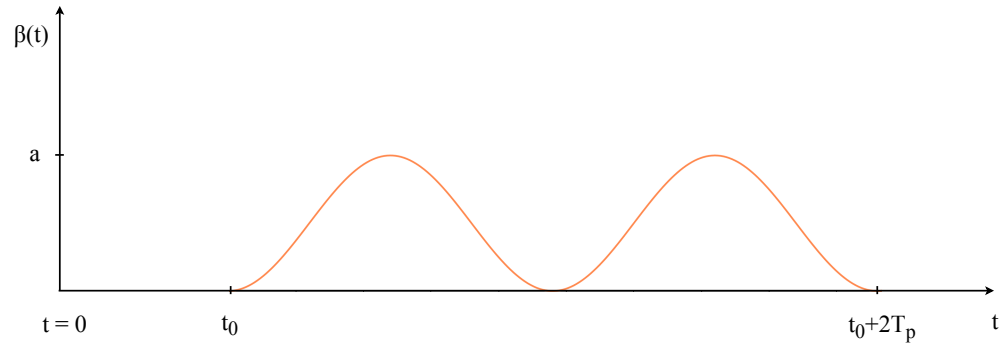

Figure 4.9: A plot of the relaxation parameter $\beta(t)$ with amplitude a, period T_p, and starting time t_0. The relaxation parameter is used to mimic consecutive events with inflow of dense water from the coast. In this illustration there are two consecutive events with inflow.

In a corresponding way, the values of the temperature are relaxed in the FRS-zone by

$$T_{FRS}(z,t) = (1-\beta(t))T_F(z) + \beta(t)T_C(z) \ . \tag{4.10}$$

The oxygen profile of the coastal water is set equal to the initial oxygen profile at the boundary in west, i.e. the outer profile of the oxygen. The coastal water is marked $\xi(x,y,z,t) = 1.0$ when arising at the western boundary.

Updating the Salinity and Temperature of the Fjord Water in the FRS-zone

When coastal water is forced into the fjord area in the FRS-zone, the fjord water in the zone is being mixed with coastal water. As a result, the properties of the fjord water in the zone will change. Thus, the fjord water in the FRS-zone must be updated each timestep. The updated value of the salinity of the fjord water is calculated by averaging over the next ten grid cells next to the FRS-zone. To avoid potential noise from the FRS-zone, two grids are left between the two zones, hence the average-zone is set to $i = 12, ..., 22$.

For all ($\forall$) cells in the j- and k-direction (width and depth of the fjord), the average values of the salinity, $\overline{S}$, in the average-zone are calculated by

$$\overline{S}(j,k) = \frac{1}{11}\sum_{i=12}^{22} S(i,j,k) \qquad \forall\ j,k.$$

In each model time step, the fjord salinity (S_F) in the FRS-zone is updated according to

$$S_F(i,j,k) = \overline{S}(j,k) \qquad \text{for } i = 1,...,10 \text{ and } \forall\ j,k.$$

The values of the fjord temperature (T_F) in the FRS-zone are updated in a corresponding way.

4.3 Bottom Water and Dissolved Oxygen

4.3.1 The Evolution of the Bottom Water

To study the evolution of the marked bottom water (ξ) with time, the volume of the remaining marked water below 300 meters depth is defined as V_θ [m^3]. At a specific time t, the volume may be calculated by

$$V_\theta(t) = \int_{\text{-300m}}^{\text{-400m}} \int_{0}^{\text{1.5km}} \int_{\text{10km}}^{\text{35.5km}} \theta(x,y,z,t)\,dx\,dy\,dz\ . \tag{4.11}$$

The remaining fraction of marked bottom water (RF) at a spesific time t is defined as

$$RF(t) = \frac{V_\theta(t)}{V_0}\ , \tag{4.12}$$

where $V_\theta(t)$ is the remaining volume at the time t, and V_0 is the initial volume of the marked bottom water.

4.3.2 The Biological Comsumption Rate of Oxygen

The dissolved oxygen concentration in the basin water is a result of the balance between the supply and consumption of oxygen. Aure and Stigebrandt (1989) state that there are three main processes that regulate the oxygen concentration of the basin water; exchange of the basin water due to inflows of coastal water denser than the basin water, vertical turbulent diffusivity, and biological consumption. However, the effect of vertical turbulent diffusivity is minor compared to the biological consumption in fjords with deep basins (Aksnes et al., 2019; Aure and Stigebrandt, 1989). Accordingly, the decay rate of oxygen is approximately equal to the biological consumption. In stagnation periods, i.e. periods with no exchange of the basin water, the dissolved oxygen in the water will be steadily consumed due to biological activity associated with the decomposition of organic matter. A simplified model to describe the change in dissolved oxygen is suggested by Aksnes *et al.* (2019),

$$\frac{\mathrm{d}O_B}{\mathrm{d}t} = R(O_S - O_B) - \bar{b} \ .$$

The average dissolved oxygen concentration of basin water is defined as O_B [ml l^{-1}], the dissolved oxygen concentration of water that intrudes into the basin as O_S [ml l^{-1}], t is time in years, and R is the renewal rate per year. An approximation of the averaged biological consumption in the basin below the sill is denoted $\bar{b}$ [ml l^{-1} year^{-1}].

In the present study, the averaged biological consumption in the basin is estimated by investigating the decline in oxygen during expected stagnation periods. Using oxygen data from the inner part of Sørfjorden, measured by NORCE, time series of the data is plotted as functions of depth as in figure 4.5. By investigating an expected stagnation period for a specific depth, b is calculated by

$$b(z) = \frac{(O_{max}(z) - O_{min}(z))}{\Delta t} \ . \tag{4.13}$$

The largest and smallest values of oxygen at that specific depth is defined as O_{max} [ml l^{-1}] and O_{min} [ml l^{-1}], respectively, and Δt [year] is the time period. Taking the average value of b for the depths below the sill level, an estimate of the biological consumption is obtained;

$$\bar{b} = \frac{1}{M} \sum_{D} b(z) \approx 0.44 \text{ ml } l^{-1} \text{ year}^{-1}. \tag{4.14}$$

Here, D is defined as the data sets from below the sill level,
$D = \{250, 275, 300, 325, 350, 375, 400\}$, and $M = 7$ is the number of depths with data.

In each model time step the dissolved oxygen in the water will decrease due to biological comsumption according to

$$O_2(i, j, k) = O_2(i, j, k) - \Delta t \cdot \bar{b} \ . \tag{4.15}$$

Thus, $\bar{b}$ is added to the model as a sink for the biological consumption.

4.4 The Eddy Viscosity and Diffusivity

In order to close the set of governing equations introduced in Chapter 2.2, the viscosity and diffusivity terms need to be specified. In the present study, the horizontal eddy viscosity (A_M) and the horizontal diffusivity (A_H) are set constant;

$$A_M = 400 \text{ m}^2\text{s}^{-1} ,$$

$$A_H = 0 \text{ m}^2\text{s}^{-1} .$$

The value of A_M is set large enough to avoid grid scale noise in the flow field, and on the other hand small enough to allow the representation of the flow in and out of the fjord. As the main focus of the present thesis is the general exchange of water between the coast and the fjord, the horizontal eddy vicosity is set relatively large. A_H is set to zero in order to minimize horizontal mixing of the tracer fields; S, T, O_2, θ, and ξ.

The vertical eddy viscosity (K_M) and the vertical diffusivity (K_H) are calculated according to the Mellor-Yamada turbulence closure scheme (Mellor and Yamada, 1982). The minimum allowed values of K_M and K_H are both set to 2×10^{-5} m^2 s^{-1}.

4.5 The Froude Number

In addition to the Richardson number, equation (2.27), the Froude number (Fr) is an important nondimensional number used to characterize the flow (Kundu et al., 2016). The Froude number is defined as the ratio between inertial forces and gravity, and Baines (1995) defines the number as

$$Fr = \frac{U}{\sqrt{g'h'}} \ , \tag{4.16}$$

where U [m s^{-1}] is the horizontal velocity of the flow, h' [m] is the flow thickness, also called height of the plume, and g' [m s^{-2}] is the reduced gravity given by

$$g' = g\frac{\Delta\rho}{\rho_0} \ . \tag{4.17}$$

Here, $g \approx 9.81$ m s^{-2} is the gravitational acceleration, $\Delta\rho$ [kg m^{-3}] is the difference in density between the two layers, and ρ_0 is the reference density set to $\rho_0 = 1000$ kg m^{-3}.

If $Fr < 1$ the flow is called *subcritical*, and if $Fr > 1$ the flow is called *supercritical*. When a flow changes from supercritical to subcritical flow, a phenomenon called *hydraulic jump* occurs (Kundu et al., 2016). The phase velocity of the waves traveling on the fluid ($\sqrt{g'h'}$) then exceeds the velocity of the fluid (U), and a rise in the height of the fluid is observed.

4.6 Numerical Simulations

In the present study three cases are considered:

- **Case 0** with the tide and no coastal inflow.
- **Case 1** with the tide and coastal inflow, without coastal warming.
- **Case 2** with the tide and coastal inflow, with coastal warming.
    - 1°C of coastal warming.
    - 2°C of coastal warming.

For each of the cases, the dynamical situation and the evolution of the marked bottom water is investigated. Table 4.1 gives an overview of the numerical simulations. Case 1 represents a situation of (partial or complete) water exchange of the basin water, with a coastal temperature corresponding to the temperature 40 years ago. A coastal warming of 1°C and 2°C represents the temperature today and with a further 1°C warming, respectively.

Case number	**Tide**	**Inflow of Coastal Water**	$T_{coast}(z)\ \forall z$
Case 0: Base Case	✓	×	×
Case 1: No coastal warming	✓	✓	7°C
Case 2:			
1°C of coastal warming	✓	✓	8°C
2°C of coastal warming	✓	✓	9°C

Table 4.1: An overview of the numerical simulations done in this study.

Initially, there is no coastal water in the fjord area (figure 4.6b). This is not realistic, as there will be some dense coastal water outside the sill due to earlier inflows from the coast. In order to allow for precondition of the model area, five inflows are let into the fjord area.

Figure 4.10 shows an illustration of the relaxation parameter used in the FRS-zone during Case 1 and Case 2. The model is running for 72 hours with only tidal force before inflows from the coast are let into the model area. The period of each inflow is set to $T_p = 72$ hours and the amplitude $a = 0.8$. A period of 72 hours could typically represent incidents of inflow from the coast due to meteorological events on the coast, e.g. northerly wind. The density profiles of the fjord and coastal water for the two main cases are plotted in figure 4.11.

In Case 0, the dynamical situation is discussed after 72 hours of tidal force. In Case 1, the situation is investigated after 1 coastal inflow, and after 5 coastal inflows. In Case 2, the situation is studied after 5 coastal inflows.

Case 0 will be a base case. The essence of the present study is to investigate how the water exchange of the bottom water may be affected by warming of the coastal water, thus the main focus of this thesis will be on Case 1 and 2. Results obtained from the numerical simulations are presented in the next chapter.

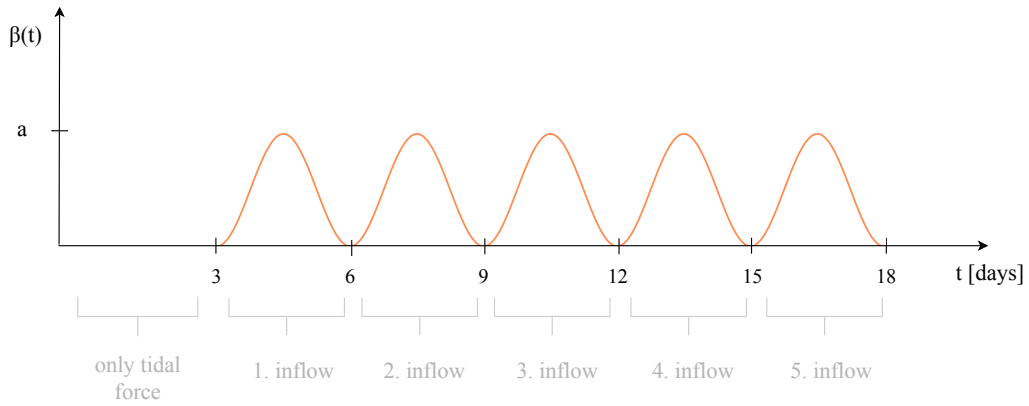

Figure 4.10: An illustration of the relaxation parameter $\beta(t)$ used in the present study. During the first 3 days only tidal force is present, thereafter inflows of coastal water occurs. The amplitude is set to $a = 0.8$ and the period of each inflow T_p =72 hours.

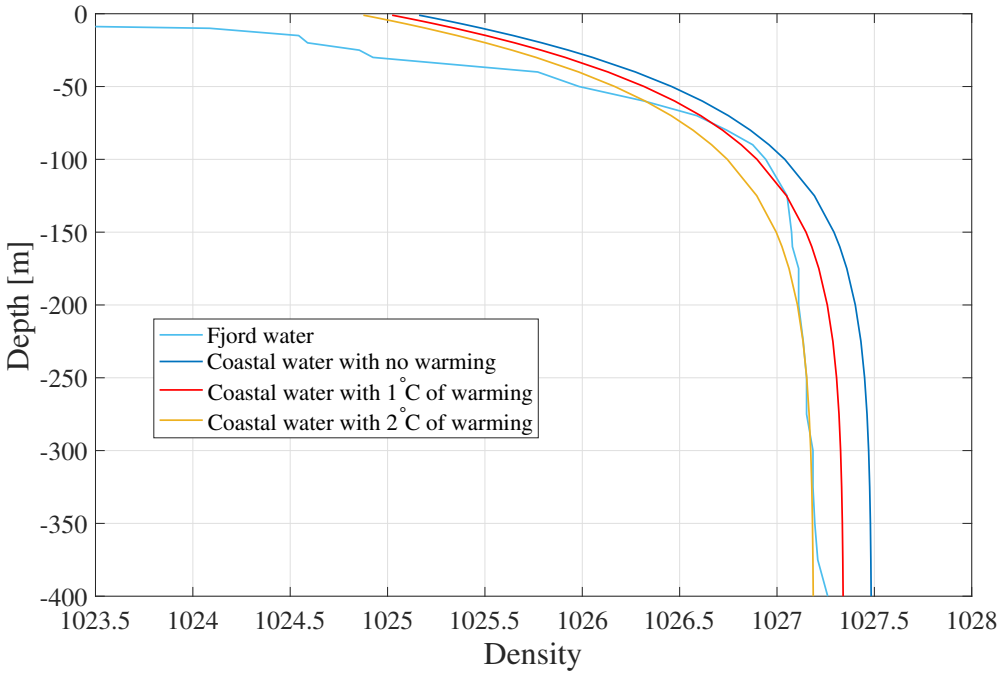

Figure 4.11: The density profile of the fjord water (light blue) and the coastal water with; no coastal warming (dark blue), 1.0°C of coastal arming (red), and 2.0°C of coastal warming (yellow).

Chapter 5

Results and Discussion

Results obtained from the numerical simulations are presented in the preceding chapter. The base case is presented in section 5.1, while results from the main cases are given in section 5.2-5.4.

5.1 Case 0: After 72 Hours with Tidal Force

Evolution of the marked bottom water

During the first 16 hours there is a period of decay of the remaining fraction of marked bottom water, due to the start-up phase of the simulation (figure 5.1). The decay then slows down, and an oscillating pattern is visible. The period of the oscillations is equal to the period of the tidal force, $T_{M_2} = 12.42$ hours. Hence, the tide moves the marked bottom water up and down.

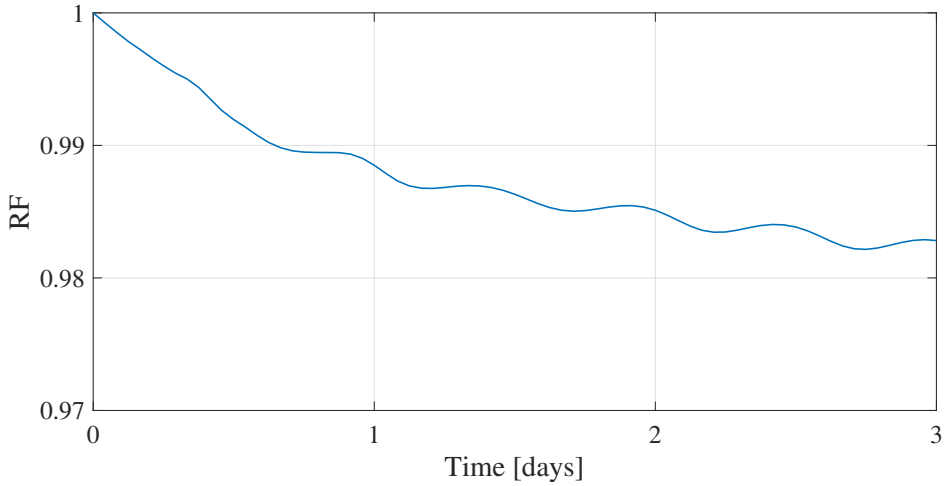

Figure 5.1: The evolution of the marked bottom water during 3 days of tidal force and no coastal inflow. The remaining fraction of the marked bottom water (RF) is plotted as a function of time.

Compared to the initial profile of the oxygen (figure 4.5), the oxygen profile after 3 days of tidal force (figure 5.2a) is almost identical. The profile of the marked bottom water (figure 5.2b) is also similar to the initial profile (figure 4.6a), but there is one visible difference; some of the marked bottom water below 300 meters depth are diluted. This is probably a result of motions in the water caused by the tide. There is also some disturbances in the marked bottom water near the inside of the sill. Part of this disturbance may be a result of the interpolating error done by MATLAB, as seen in figure 4.6. But velocities in the water due to the tidal force may also contribute (figure 5.3a). A positive horizontal velocity can be observed near the inner part of the sill, moving marked bottom water away from the sill. Positive and negative velocities are also generated in the upper 100 meters. There are no substantial differences in the density profile from the initial profile (figure 4.4), but some minor bending in the contour lines near the sill are observed (figure 5.3b). This is probably also a result of movements in the water back

and forth caused by the tidal force.

After 72 hours of only tidal force, 1.7 % of the marked bottom water has been replaced by ambient water. Based on this base case and results from previous simulations over a longer period of time (Sand, 2018), it is apparent that the tidal force moves the basin water back and forth, but has no significant effect on the exchange of the marked bottom water.

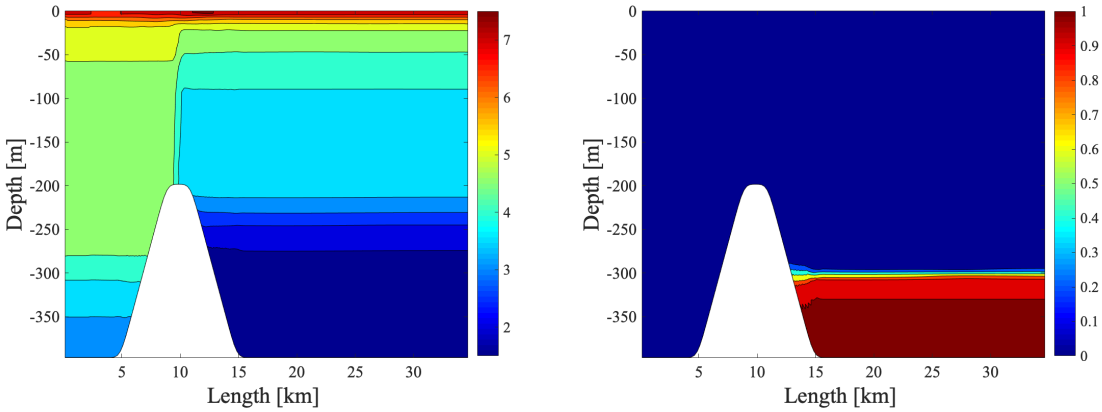

Figure 5.2: Contour plots of the (a) oxygen, O_2 [ml l^{-1}], and (b) θ-tracer, marking the bottom water, after 3 days with tidal force and no coastal water.

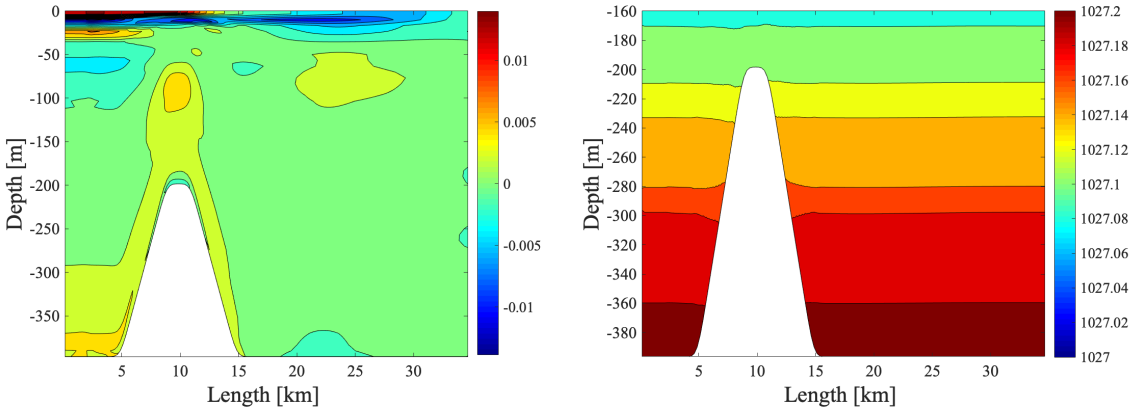

Figure 5.3: Contour plots of the (a) horizontal velocity, U [m s^{-1}], and (b) density, ρ [kg m^{-3}], after 3 days with tidal force and no coastal inflow. Only the lower 240 meters are plotted in (b), as the area around the sill is the area of interest.

5.2 Case 1: No Coastal Warming

After 1 Inflow of Coastal Water

In order to investigate the dynamics near the sill and fjord basin during the first coastal inflow, the inflow is divided into four stages; $T_{\frac{1}{4}}$, $T_{\frac{2}{4}}$, $T_{\frac{3}{4}}$ and T_1. These stages correspond to 3.75, 4.5, 5.25 and 6.0 running days of the model, respectively (figure 5.4). The four stages will be used in the rest of this section to investigate the dynamics in the fjord model during the first inflow.

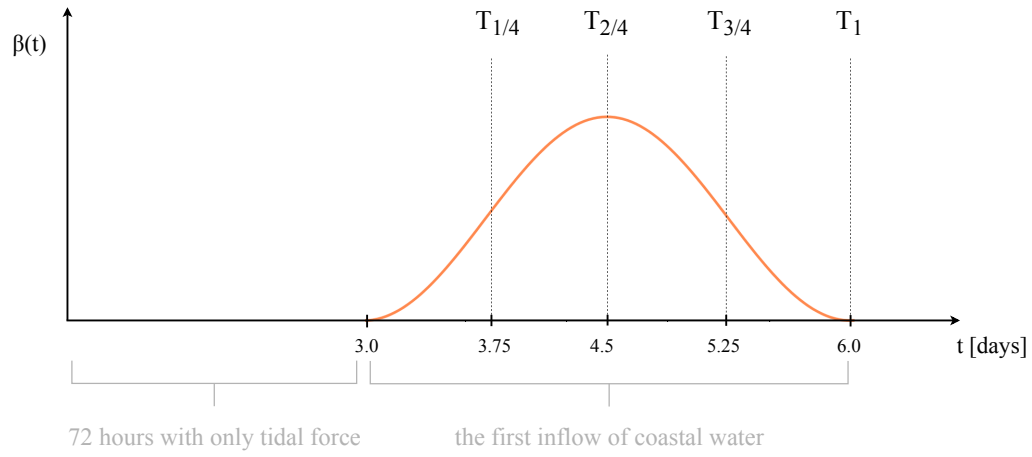

Figure 5.4: The first coastal inflow is divided into four stages; $T_{\frac{1}{4}}$, $T_{\frac{2}{4}}$, $T_{\frac{3}{4}}$ and T_1.

Evolution of the marked bottom water

Around 12 hours into the first inflow, the fraction of remaining marked bottom water (4.12) starts to decrease, and a strong exponential decay is visible from day 4 (figure 5.5). The most dramatic decay happens during stage $T_{\frac{2}{4}}$. The decay then slows down during the last two stages. After six days

the remaining amount of marked bottom water in the lower 100 meters has decreased to 39.1% of the initial volume.

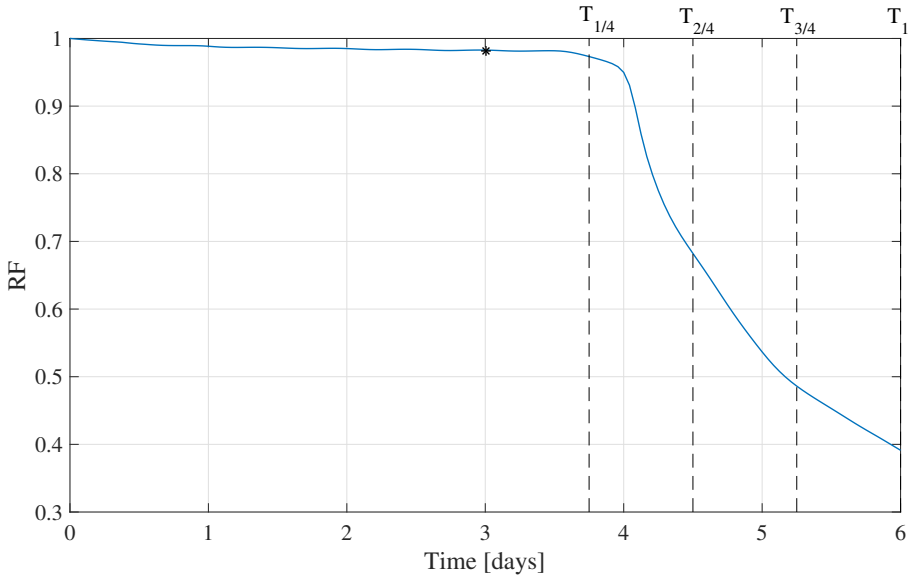

Figure 5.5: The remaining fraction of the marked bottom water (RF) plotted against time, during 3 days of tidal force and thereafter one coastal inflow. The start of the first inflow is marked with a star "*".

The density profile during the first inflow

During the first stage, $T_{\frac{1}{4}}$, dense coastal water is visible in the FRS-zone (figure 5.6a). The coastal water is moving towards the outer part of the sill, pushing water towards the sill. As a result, some of the water initially situated on the sill, are moving over the sill into the fjord basin. This is visible in the bending of the density contours behind the sill in figure 5.6a.

During stage $T_{\frac{2}{4}}$, denser coastal water quickly builds up outside the sill, pushing dense water over the sill and into the fjord basin (figure 5.6b). Water of greater density than the lower basin water decends from the top of the sill and down to the bottom of the basin. Thus, some time between the

first and second stage, dense water has begun to move over the sill. This continues through stage $T_{\frac{3}{4}}$ and T_1 (figure 5.6c-5.6d). At stage T_1, dense water has moved over to the east boundary, moving along the bottom of the fjord basin.

Initially, the density profile in the fjord is stable, i.e. $\frac{\partial \rho}{\partial z} \leq 0$ (figure 4.4). In this stable state, water parcels are in their equilibrium position, at the same depth as other parcels of equal density. When dense water moves over the sill and into the basin, water parcels situated in the basin will be pushed away from the equilibrium positions. This is visible behind the sill at stage $T_{\frac{1}{4}}$, resulting in bending of the density contours (figure 5.6a). Particles displaced downward from the equilibrium position is less dense than its surroundings. The system will try to restore the equilibrium; the water parcels experience a buoyancy force upwards and start oscillating around the equilibrium position due to having momentum. This oscillating behavior, making disturbances in the density contours, can be seen behind the sill during stages $T_{\frac{2}{4}}$-T_1 (figure 5.6b-d). These small perturbations generate internal waves in the fluid (Cushman-Roisin and Beckers, 2011).

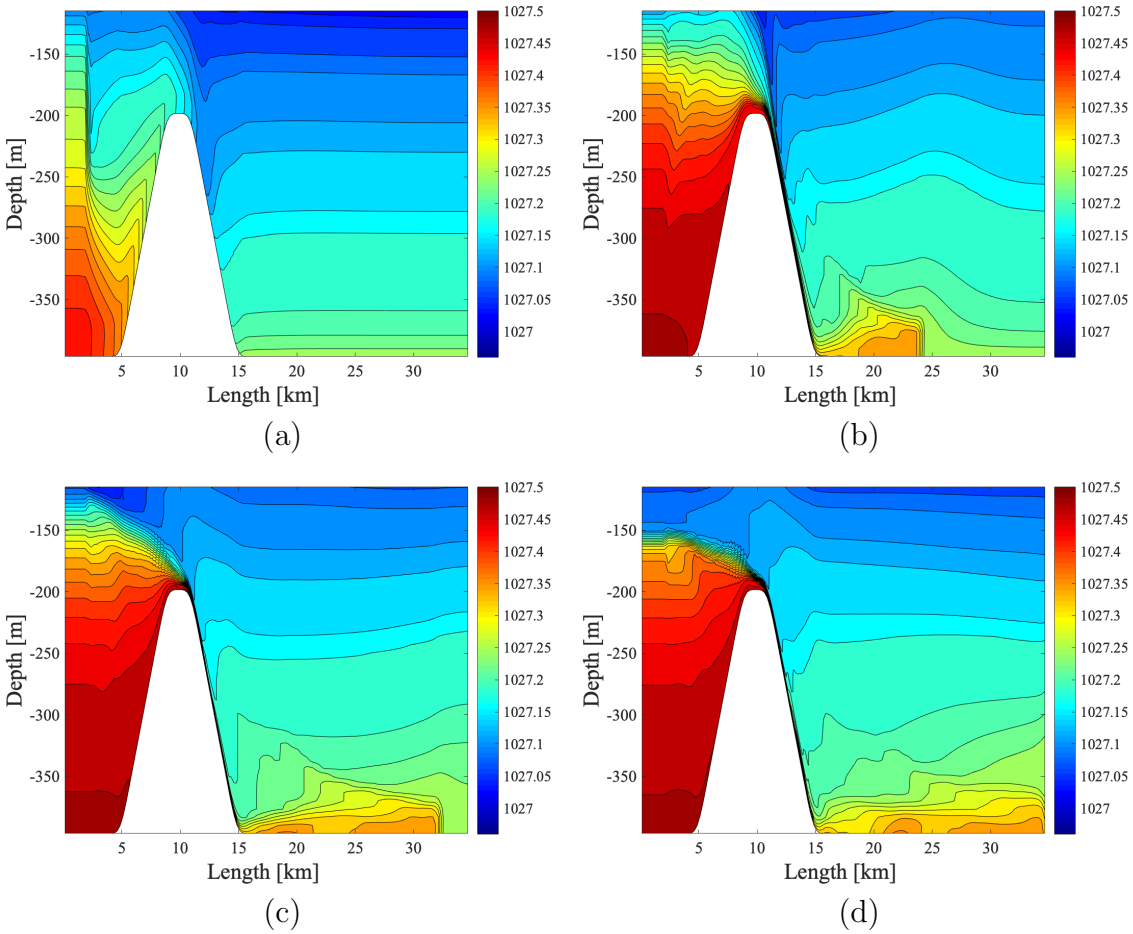

Figure 5.6: Contour plots of the density, ρ [kg m^{-3}], at stage (a) $T_{\frac{1}{4}}$ (b) $T_{\frac{2}{4}}$ (c) $T_{\frac{3}{4}}$ and (d) T_1. Only the lower 340 meters are plotted as the area around the sill is of interest.

During the first three days with only tidal force, there are only minor oscillating disturbances in the density contours over the sill (figure 5.7). Around 12 hours into the first inflow a rise of the density contours is observed, hence dense water is moving over the sill surface. This compares well with the first event of dense water flowing over the sill, between stage $T_{\frac{1}{4}}$ and $T_{\frac{2}{4}}$ (figure 5.6). The period of the tide is visible as oscillating patterns in the contour

lines.

To study how the inflows from the coast influence the water in the fjord, the density change in the model area is of interest. The change in density after n inflows, compared to after 72 hours of tidal force, is denoted by $\Delta\rho_n$ and may be calculated by

$$\Delta\rho_n = \rho(72 + n \cdot T_p) - \rho(72) \ . \tag{5.1}$$

Here, $\rho(72)$ is the density profile after 72 hours with only tidal force, and $\rho(72 + n \cdot T_p)$ is the profile after n inflows of coastal water.

After 1 coastal inflow a density increase is observed on the outside of the sill, due to the built up of dense water (figure 5.8a). Smaller density changes are found in the fjord basin (figure 5.8b). Near the bottom of the basin, there are areas of density increase, a result of the dense water moving over the sill and into the basin. Water moving over the sill push water parcels situated in the basin downward from the equilibrium positions. This may explain the areas of negative density change by the inner part of the sill. Positive changes in density are visible around 100 meters depth. Flows of dense coastal water moving into the fjord increase the density in areas near the water surface.

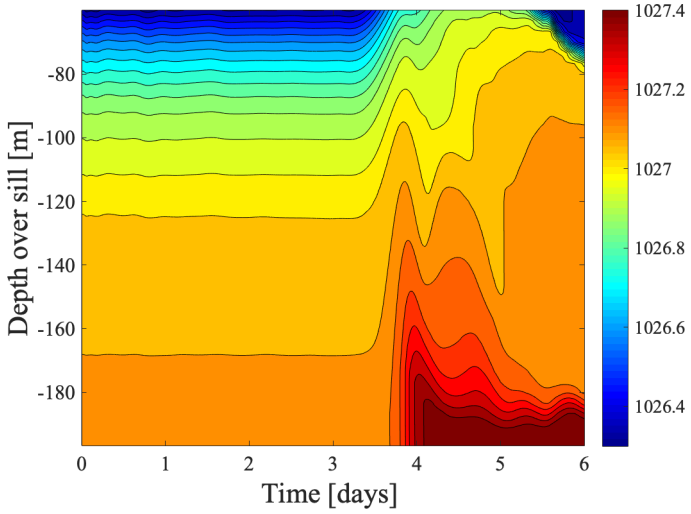

Figure 5.7: Time series of the density, ρ [kg m^{-3}], above the sill. During the first 3 days only tidal force is present, thereafter one inflow of coastal water occurs. Only the lower 140 meters are plotted, as the area near the sill surface is of interest.

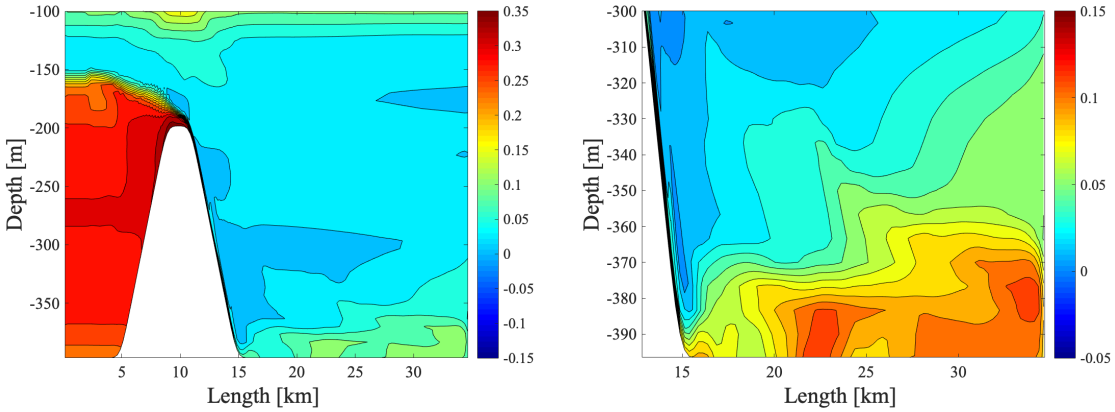

(a) (b)

Figure 5.8: Contour plots of the change in density after one coastal inflow compared to after 3 days of only tidal force, $\Delta\rho_1$ [kg m^{-3}]. Only the lower 300 meters are plotted in (a), as the area near the sill surface is of interest. The lower 100 meters of the fjord basin is plotted in (b).

The horizontal velocity profile during the first inflow

The pressure is dependent on the surface elevation (η) and the density (ρ) through equation (2.13). Accordingly, the pressure gradient in the x-direction is dependent on $\frac{\partial \eta}{\partial x}$ and the depth integrated $\frac{\partial \rho}{\partial x}$. As the tidal force is weak, $\frac{\partial \eta}{\partial x}$ is negligible. Consequently, the dynamics in the model area is dominated by the depth integrated density gradient, together with the continuity equation (2.4), i.e. conservation of volume.

At the first stage, $T_{\frac{1}{4}}$, a positive horizontal velocity is visible in the lower 100 meters outside the sill (figure 5.9a). The flow is moving up the outer part of the sill, towards the sill top. The positive velocity is compensated by a negative velocity out of the fjord, which is strongest in the upper 50 meters. This flow is induced to conserve volume; when water moves into the fjord area, some water must move out of the fjord.

At stage $T_{\frac{2}{4}}$, there is a strong positive horizontal velocity from the top of the sill, moving down towards the fjord basin (figure 5.9b). This is the velocity of dense water moving down the inner part of the sill, as observed in figure 5.6b. Areas of weak negative velocity, compensating for the positive velocity, can be observed, particularly in the upper 100 meters.

At stage $T_{\frac{3}{4}}$, a strong flow into the fjord is observed in the upper 50 meters, west in the model area (figure 5.9c). This flow is generated by the density difference between the fjord and coastal water, see figure 4.8. The density gradient creates a flow in order to balance out the difference in density. The density gradient is largest near the water surface, hence this is where the flow occurs. The flow into the fjord is compensated by a negative velocity around 50-150 meters depth, directed out of the fjord. Due to mixing of fjord and coastal water during the first inflow, the density gradient in the next inflow is expected to be considerably weaker.

The velocity into the fjord due to the density gradient is smaller, but present in stage T_1 (figure 5.9d). A weak negative velocity directed out of the fjord is also observed in the upper 15 meters of the fjord. A velocity down the inner part of the sill is still visible during stage $T_{\frac{3}{4}}$-T_1, but is strongest in the stage $T_{\frac{2}{4}}$.

The density profiles for the fjord and coastal water (figure 4.11) may indicate possible flows induced by the density gradients. However, the profiles might change into the model area, as they are only initial profiles.

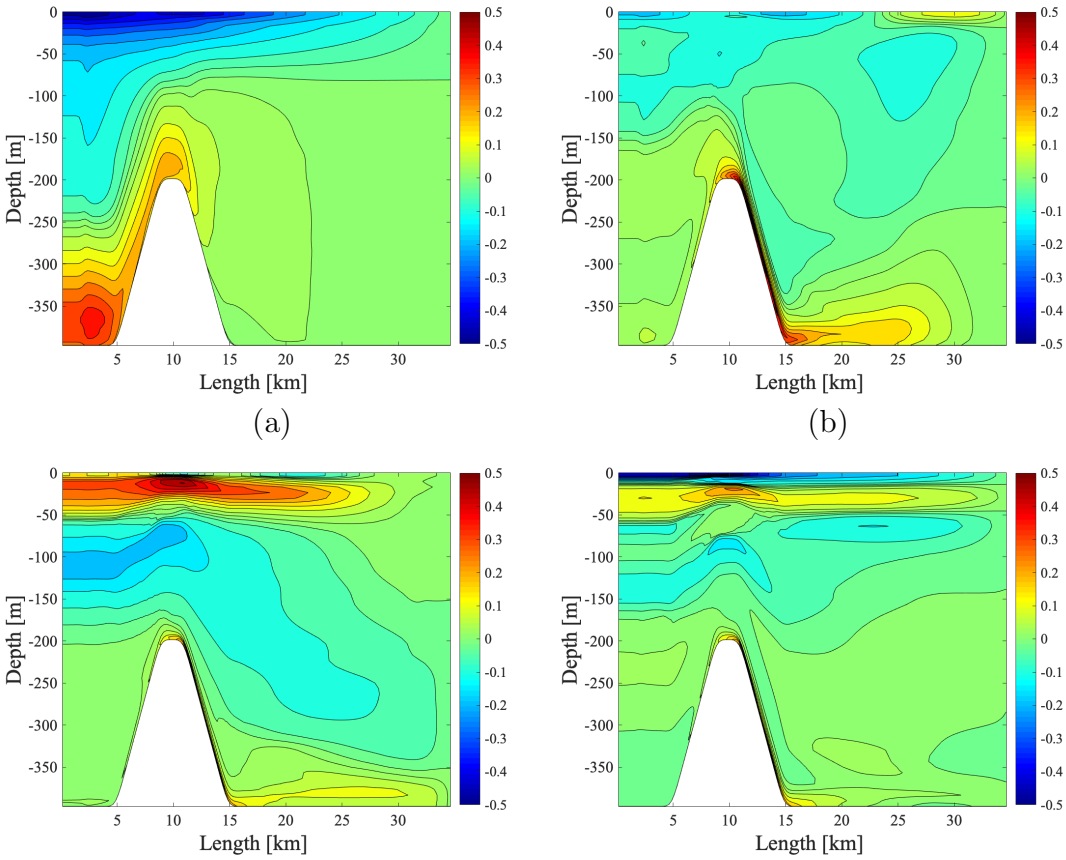

Figure 5.9: Contour plots of the horizontal velocity, U [m s^{-1}], at stage (a) $T_{\frac{1}{4}}$ (b) $T_{\frac{2}{4}}$ (c) $T_{\frac{3}{4}}$ and (d) T_1 during the first coastal inflow.

During the first three days with only tidal force, there are regular horizontal movements in the fluid above the sill (figure 5.10). This is a result of the tidal force, moving the water back and forth. Around 12 hours into the inflow a positive velocity over the sill surface is observed, together with a compensating negative velocity out of the fjord near the water surface. This compared well with the time of the first flow of dense water over the sill surface, as seen in figure 5.7.

During day 5-6, the flow generated by the density gradient between the fjord and coastal water is visible in the upper 40 meters and the compensating negative flow is observed around 60-160 meters depth. The model results in figure 5.10 is consistent with the model results in figure 5.7 and 5.9.

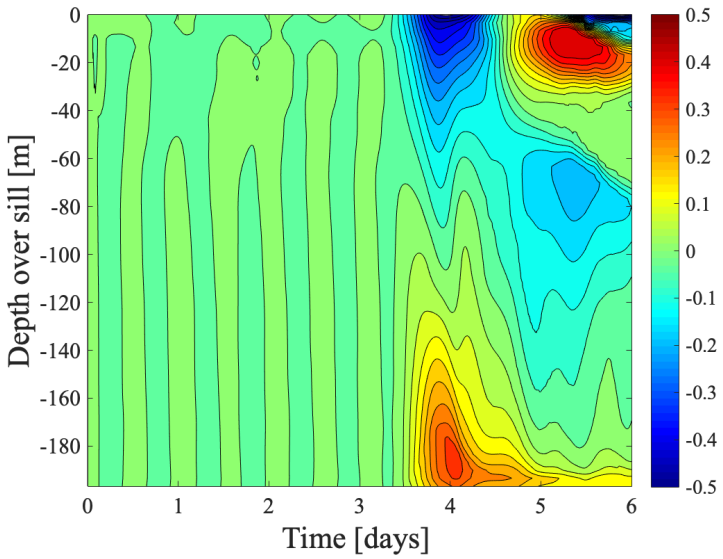

Figure 5.10: Time series of the horizontal velocity, U [m s^{-1}], above the sill. During the first 3 days only tidal force is present, thereafter one inflow of coastal water occurs.

As the horizontal velocity of the fluid increase down the upper inner part of the sill, the Froude number (4.16) also increase (figure 5.12a and 5.11). The estimate of the Froude number indicates that a transition from subcritical to supercritical flow occurs at the inner part of the sill around 1 kilometers from the sill top. The velocity slows down and starts decreasing, and 4-5 kilometers from the top of the sill the flow changes from a supercritical to a subcritical regime. Fluid with high velocity flows into an area of less veloctiy, and a hydraulic jump is observed as a increase in height of the plume moving down the sill surface (figure 5.12b). Due to mass conservation the volume flow rate per unit width in the plume must be equal before and after the hydraulic jump (Kundu et al., 2016),

$$Q = U_1 h_1' = U_2 h_2' \ . \tag{5.2}$$

Here, Q [$\mathrm{m}^3\ \mathrm{s}^{-1}$] is the volume flow rate per unit width that is normal to a cross sectional surface. The horizontal velocities U_1 and U_2, and the heights h_1' and h_2', are the velocity and the height of the fluid plume before and after the hydraulic jump, respectively. During the hydraulic jump, the velocity of the fluid decreases, $U_1 > U_2$. Therefore, in order to conserve mass the height of the plume must increase, hence $h_1' < h_2'$ (figure 5.12b).

In theory hydraulic jumps occur instantaneously, but due to viscosity and diffusivity, the jump arise more gradually in the numerical simulations. As the main focus in this thesis is the general dynamics in the model area, the grid resolution near the sill surface is low. Consequently, the plotted Froude number is a very rough estimate. Furthermore, the velocity in the plume is not vertical homogeneous, due to viscosity and diffusivity.

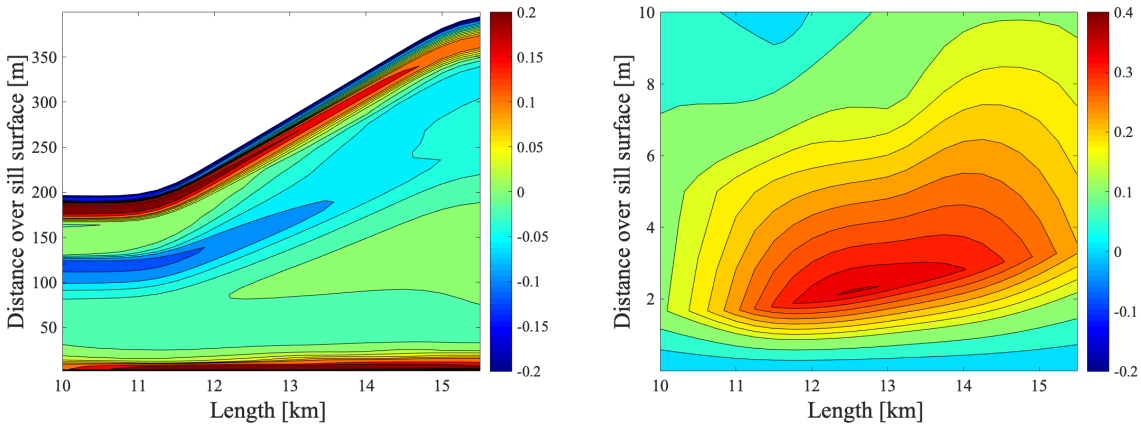

(a) (b)

Figure 5.11: Profiles of the horizontal velocity, U [m s^{-1}], down the inner part of the sill. In (a) the entire depth above the sill is plotted, while only the lower 10 meters are plotted in (b).

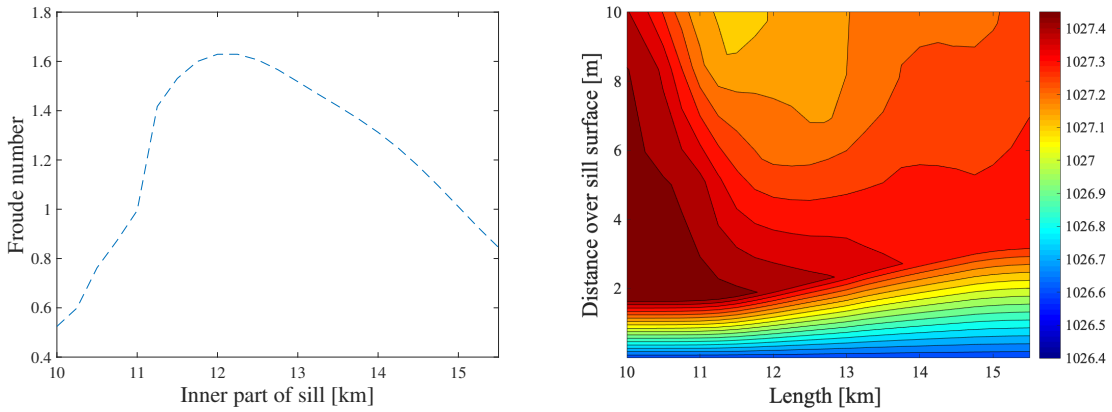

(a) (b)

Figure 5.12: A rough estimate of the Froude number (4.16), down the inner part of the sill, is plotted in (a), while a contour plot of the density, ρ [kg m^{-3}], in the lower 10 meters above the sill is plotted in (b).

The vertical velocity profile during the first inflow

As dense water moves up the outer part of the sill, a positive vertical velocity is observed at stage $T_{\frac{1}{4}}$ (figure 5.13). Due to flow of water over the sill top, a negative vertical velocity is visible down the upper inner part of the sill. During stage $T_{\frac{2}{4}}$, dense water builds up outside the sill and begins to flow over the sill, resulting in a weaker positive velocity up and a strong negative velocity down the sill. Due to the build up of dense water, the strength and height of the positive velocity becomes weaker during stages $T_{\frac{2}{4}}$-T_1. The negative velocity down the inner part of the sill is largest at stage $T_{\frac{2}{4}}$, and decrease in strength and thickness towards stage $T_{\frac{3}{4}}$, with no apparent changes between stage $T_{\frac{3}{4}}$ and T_1.

During the first three days, tidal motion in the water is visible in the vertical velocity profile at three positions on the sill (figure 5.14a-d). Around 12 hours into the first inflow a positive vertical velocity is observed at position I (figure 5.14a). As water is moving over the sill it will push away water situated near the sill, resulting in a positive vertical velocity around day 3.5-4. The water that has been lifted moves down again. Hence, the positive velocity is followed by a negative velocity during day 4-5. These positive and negative vertical velocities are also visible at the two other positions on the sill (figure 5.14b-c). However, the two consecutive velocities occur some hours later and they appear stronger, particularly at position II. This may be explained by an increase of momentum of the water when flowing down the inner part of the sill. When water moves from the sill and into the fjord basin, the density contours are disturbed, resulting in oscillations in the interior, $\frac{\partial \rho}{\partial x} \neq 0$. This cause small vertical movements in the vertical velocity profiles.

The vertical velocity profile during the first inflow is consistent with the density and horizontal velocity profile (figure 5.6 and 5.9).

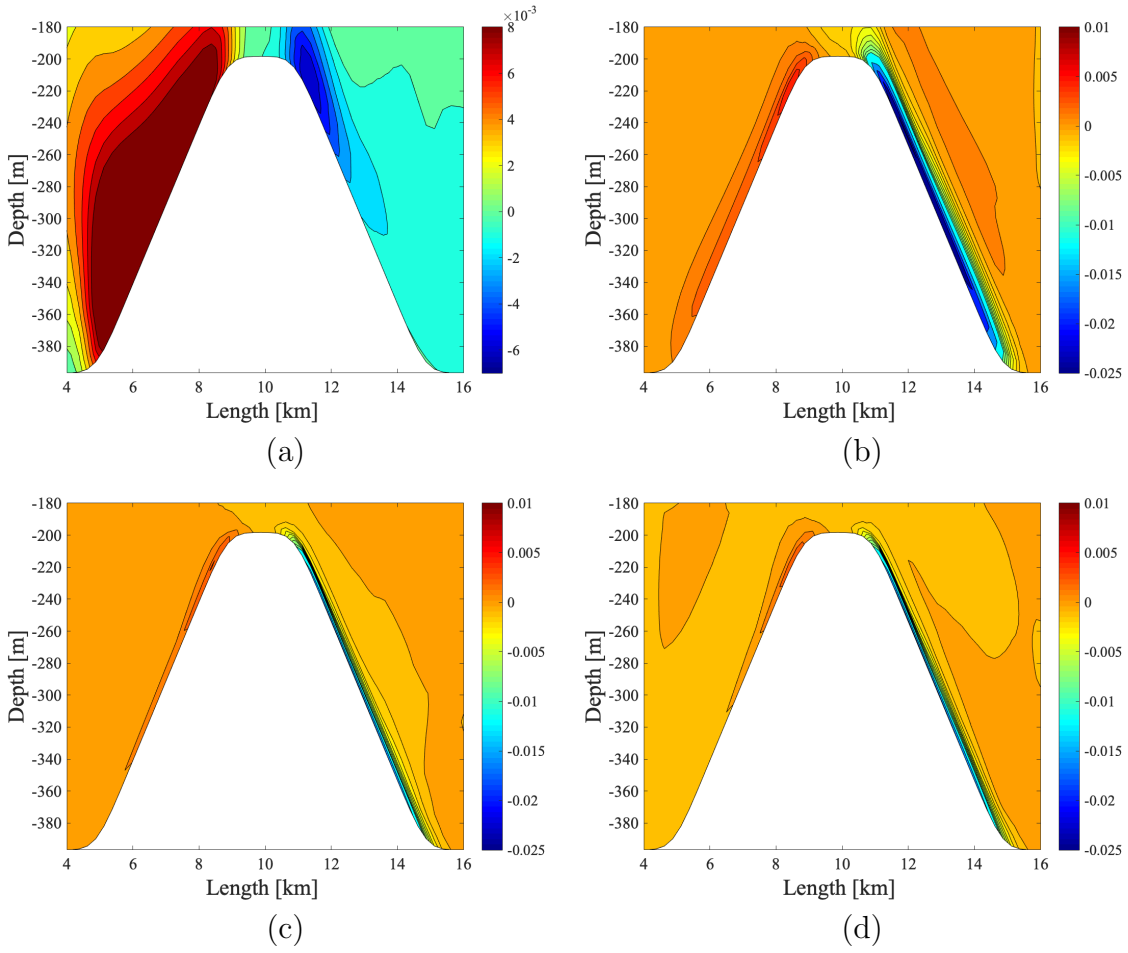

Figure 5.13: Contour plots of the vertical velocity, W [m s^{-1}], at stage (a) $T_{\frac{1}{4}}$ (b) $T_{\frac{2}{4}}$ (c) $T_{\frac{3}{4}}$ and (d) T_1 during the first coastal inflow. Only the area near the sill is plotted, as this is the area of interest. Remark: The contour levels in figure (a) is different than the contour levels in figure (b), (c), and (d).

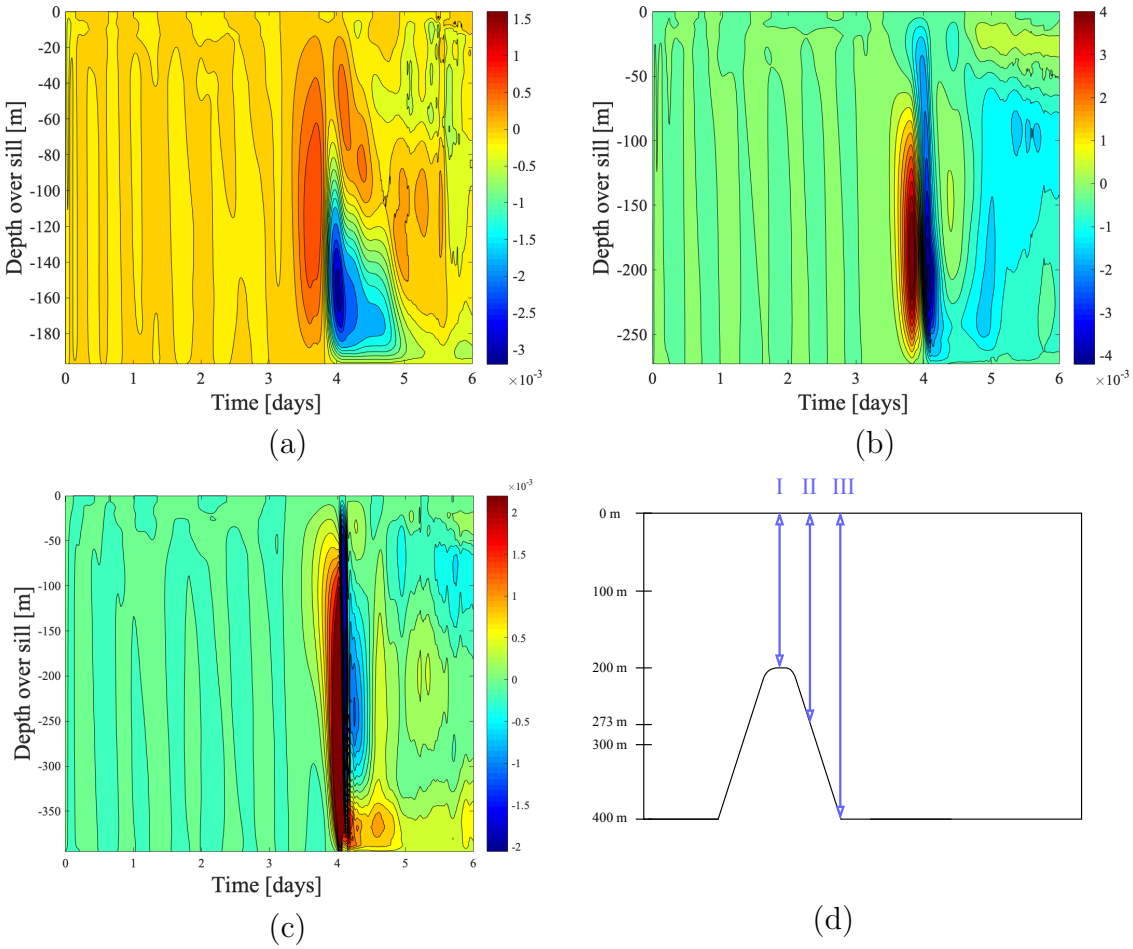

Figure 5.14: Time series of the vertical velocity, W [m s^{-1}], at position (a) I (b) II and (c) III. Figure (d) illustrates the three locations (I, II, and III) on the sill. They are located approximately 0, 2.75, and 5.5 kilometers from the sill top, respectively. Remark: the contour levels in the figures are different.

Contours of the passive tracers during the first inflow

As coastal water moves into the model area, some of the dense water descends towards the lower 200 meters outside the sill (figure 5.15). Dense coastal water builds up outside the sill, pushing fjord and coastal water over the sill and into the fjord basin. At stage T_1 coastal water has reached the eastern boundary, moving along the bottom of the fjord basin. The horizontal velocity in the upper 60 meters, induced by the density gradient between the fjord and coastal water, transports coastal water towards the inner part of the fjord (figure 5.15c-d).

As dense water is flowing down the inner part of the sill at stage $T_{\frac{2}{4}}$, the water intrudes into the basin water and down to the bottom of the basin (figure 5.16 and 5.17). The water moves down to the bottom of the basin and towards the eastern boundary. As a result, oxygen-depleted basin water arises from the bottom.

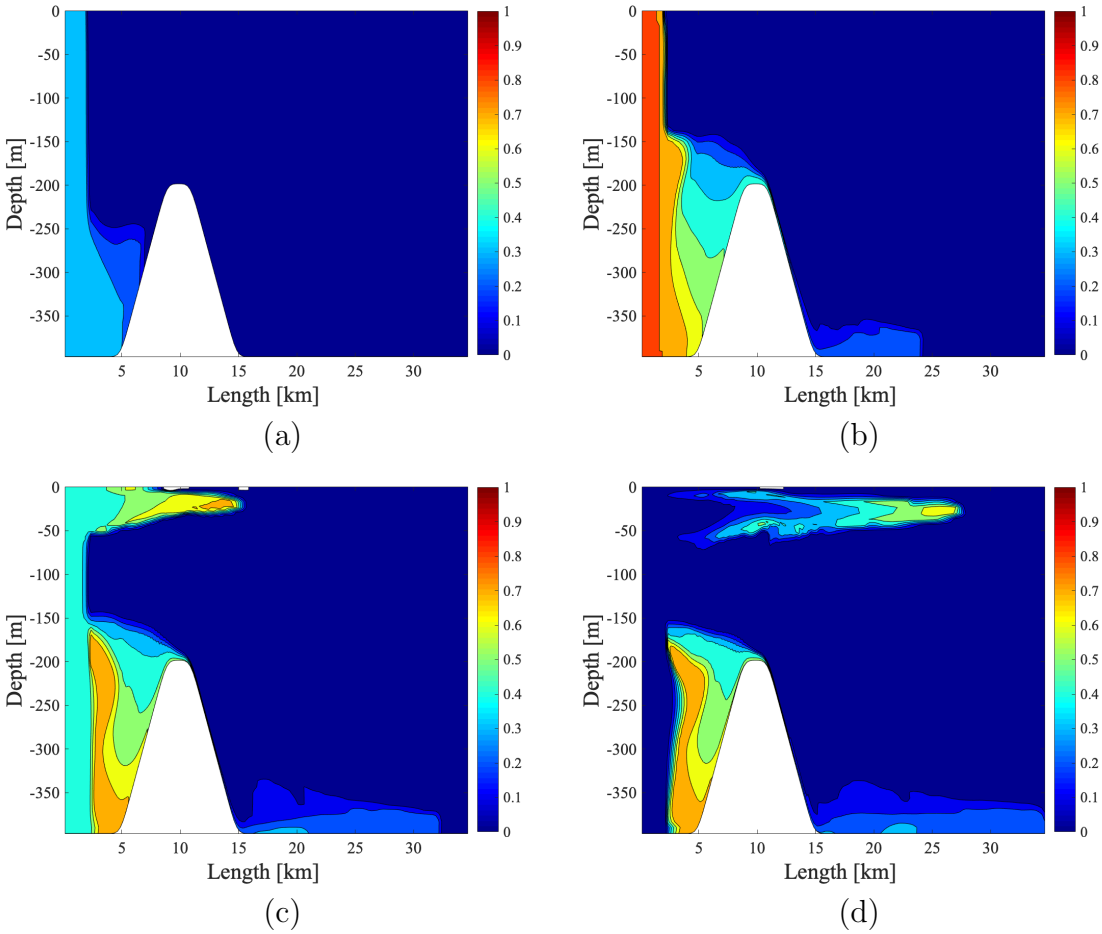

Figure 5.15: Contour plots of the ξ-tracer, marking the the coastal water, at stage (a) $T_{\frac{1}{4}}$ (b) $T_{\frac{2}{4}}$ (c) $T_{\frac{3}{4}}$ and (d) T_1 during the first coastal inflow.

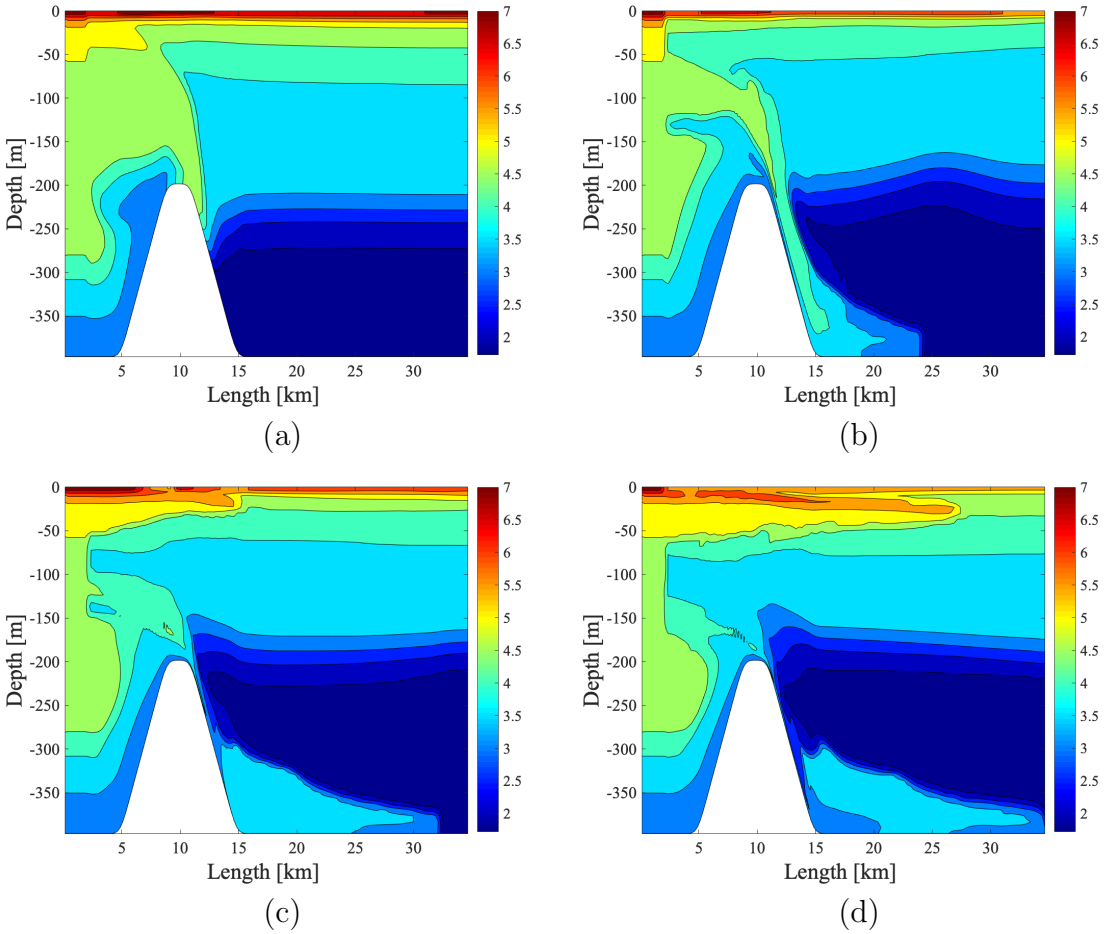

Figure 5.16: Contour plots of the oxygen, O_2 [ml l^{-1}], at stage (a) $T_{\frac{1}{4}}$ (b) $T_{\frac{2}{4}}$ (c) $T_{\frac{3}{4}}$ and (d) T_1 during the first coastal inflow.

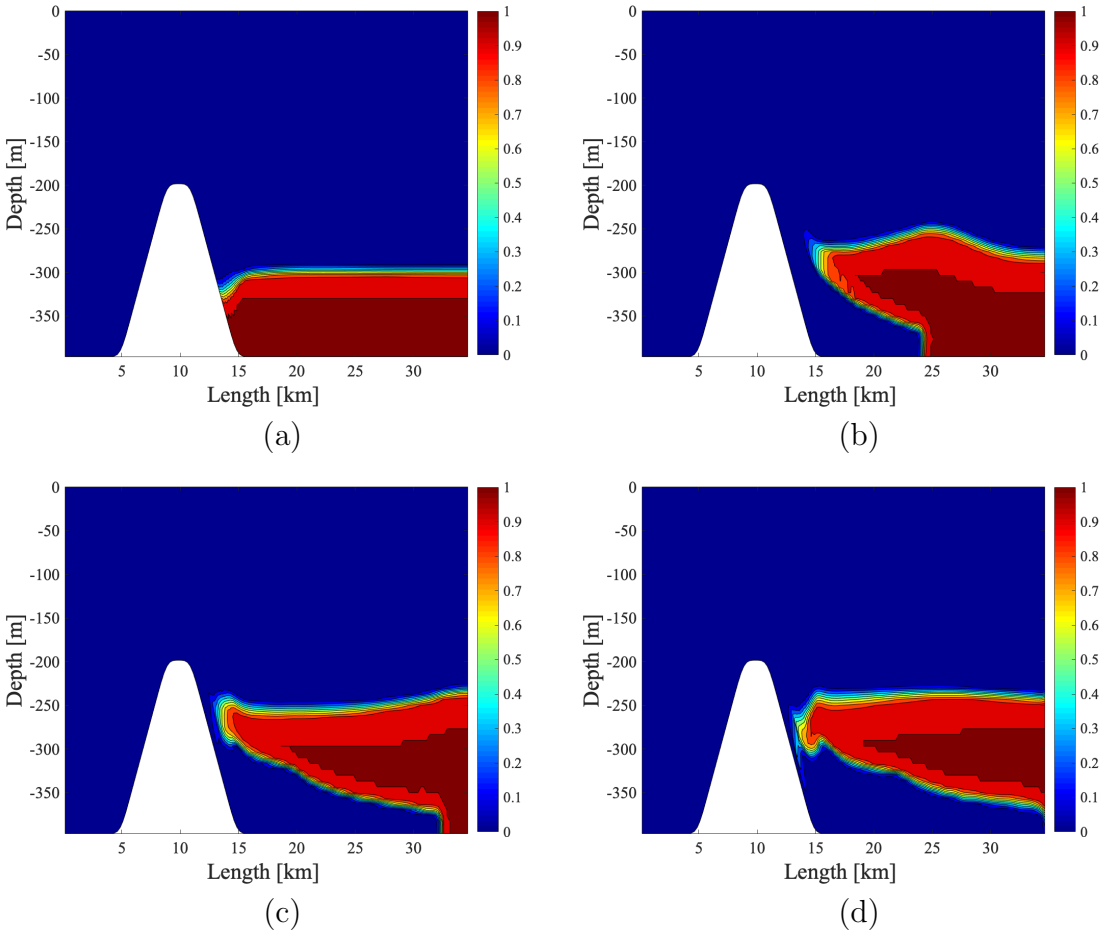

Figure 5.17: Contour plots of the θ-tracer, marking the bottom water, at stage (a) $T_{\frac{1}{4}}$ (b) $T_{\frac{2}{4}}$ (c) $T_{\frac{3}{4}}$ and (d) T_1 during the first coastal inflow.

After 5 Inflows of Coastal Water

Evolution of the marked bottom water

The decrease of remaining fraction of marked bottom water (RF) from the first inflow continues for a couple of hours, before the decay stops, and then starts to decrease again around day 7 (figure 5.18). Towards the end of the second inflow, the decay slows down. During the third inflow, there is a steady decrease of RF, before it reaches a low around day 12. At the start of the fourth inflow, 95.3% of the initial marked basin water has been replaced. During the last two inflows there is an gradually increase of RF.

There are two external forces present in this situation; the tidal force and inflow from the coast. These forces move in different phases and interact with each other. The stop in decrease of RF around 6 hours into the second inflow is probably a result of the two forces arriving out of phase, canceling each other out. The strong decay during the first inflow may be a result of the two forces strengthening each other.

After only two coastal inflows, 88.1 % of the marked bottom water has been replaced by ambient water. After five inflows, 92.8 % has been replaced.

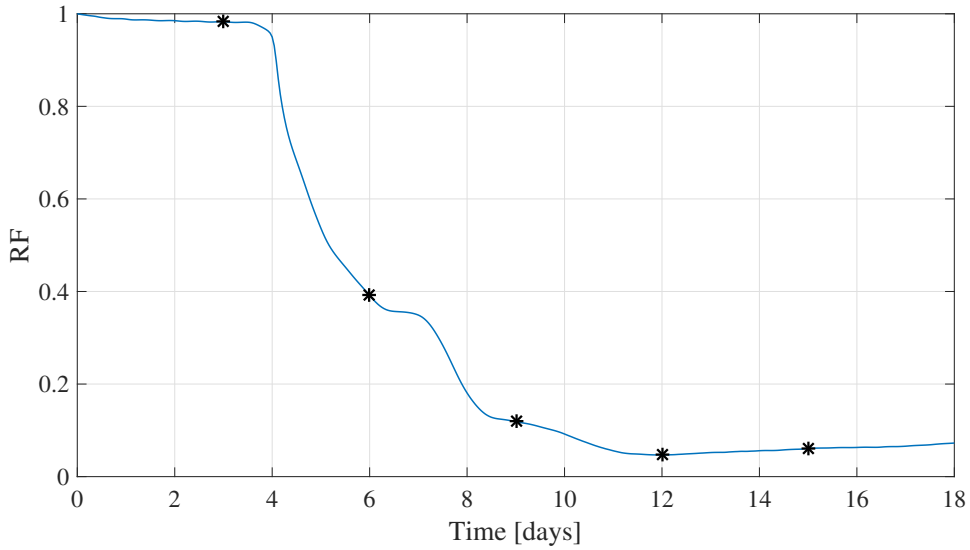

Figure 5.18: The remaining fraction of the marked bottom water (RF) plotted against time, during 3 days of tidal force and thereafter five coastal inflows. The starting time of an inflow is marked with a star ("*").

The density profile

Similarly to the situation after one coastal inflow, dense water has built up outside the sill (figure 5.19). The size of the increase outside the sill is similar (figure 5.20). However, a larger density increase is observed in the basin after 5 inflows. The four bundles of dense water, visible in the basin, may be a result of the first four inflows (figure 5.20b). A fifth can be seen near the inside of the sill surface. The area of density increase in the basin water suggests a considerable intrusion of dense water caused by the inflows.

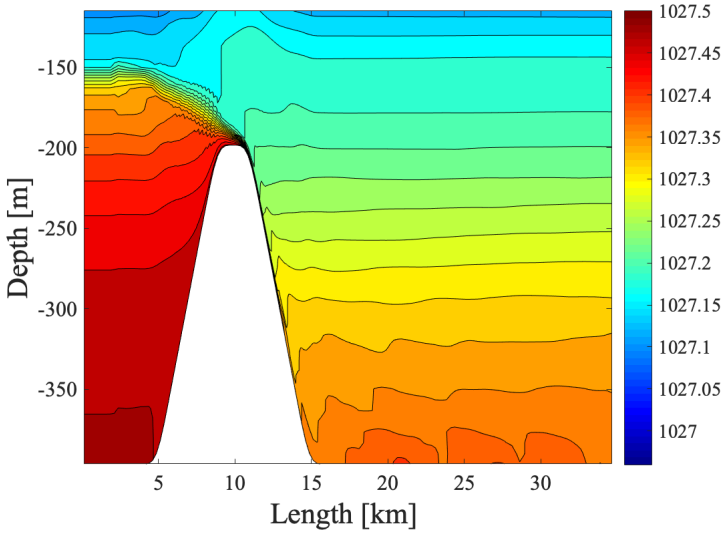

Figure 5.19: Contour plots of the density, ρ [kg m^{-3}], after five coastal inflows. Only the lower 285 meters are plotted as the area around the sill is of interest.

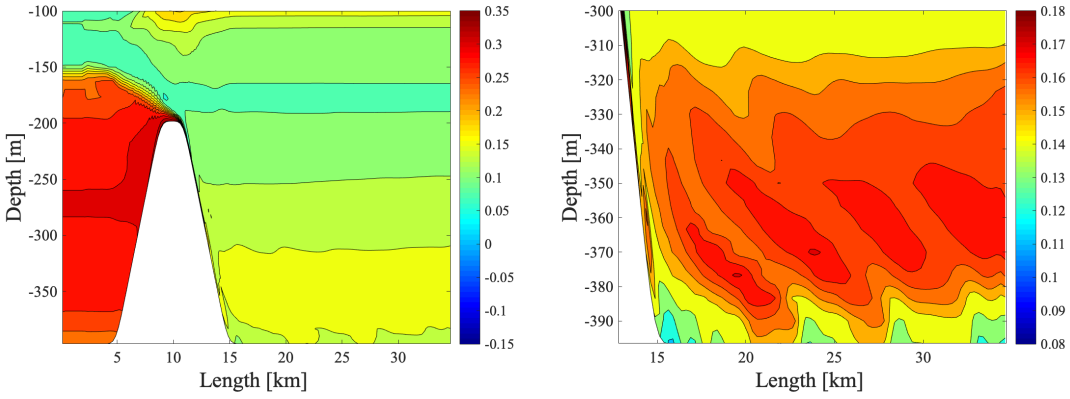

(a) (b)

Figure 5.20: Contour plots of the change in density after five coastal inflows compared to after 3 days of only tidal force, $\Delta\rho_5$ [kg m^{-3}]. Only the lower 300 meters of the model area is plotted in (a), as the area near the sill surface is of interest. The lower 100 meters of the fjord basin is plotted in (b).

During the last four inflows, oscillating patterns in the density contours over the sill are observed (figure 5.21). The oscillations consisting of four periods, correspond to each of the four inflows. Oscillations with the same period as the tidal force are visible on the oscillations from the inflows, especially near the surface of the sill. This is internal waves with the frequency of the tide, called *internal tides* (Cushman-Roisin and Beckers, 2011). They are generated by the surface tide and propagates into the fjord. The increase of the density contours in the lower 170 meters, particularly after the first inflow, indicate that the density profile over the sill is raised, and that dense water is flowing over the sill. This is consistent with figure 5.20a.

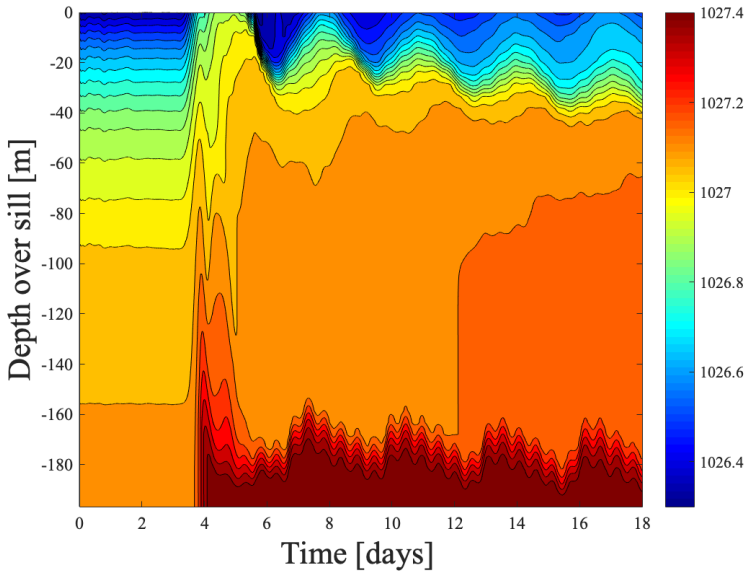

Figure 5.21: Time series of the density, ρ [kg m^{-3}], above the sill. During the first 3 days only tidal force is present, thereafter five inflows of coastal water occur.

The horizontal velocity profile

The horizontal velocity, induced by the density gradient between the fjord and coastal water in the upper 40 meters, appears to be considerably weakened during the last four inflows (figure 5.22). This was expected, as the density gradient is weakened by the mixing of fjord and coastal water in the model area. Consequently, the compensating negative velocity around 70-120 meters depth is also weaker.

The horizontal velocity near the sill surface decrease during the last four inflows, resulting in a weaker compensating negative velocity close to the water surface. This weakning is probably also a result of a smaller density gradient. Patterns corresponding to the tidal period are still observed in the velocity profile.

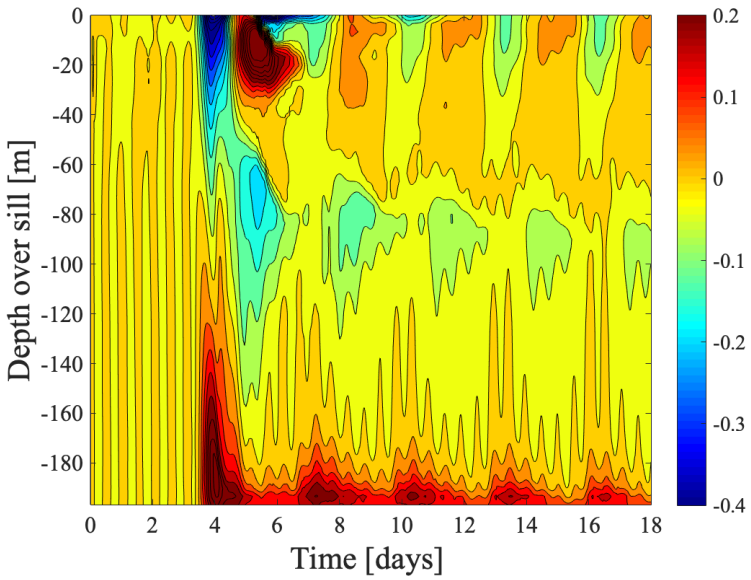

Figure 5.22: Time series of the horizontal velocity, U [m s^{-1}], above the sill. During the first 3 days only tidal force is present, thereafter five inflows of coastal water occur.

Estimates of the Froude number (4.16) down the inner part of the sill indicate a transition from subcritical flow to supercritical flow around 500 meters from the sill top (figure 5.24a). This compares well with a increase of horizontal velocity (figure 5.23b). Around 1.5 kilometers from the top, the Froude number starts to decrease, and a transition to subcritical regime occurs close to 3 kilometers from the top of the sill. A hydraulic jump occurs. The increase in plume height (h') happens as the flow moves into an area of less velocity (figur 5.23). Due to viscosity and diffusivity, the increase in height of the plume happens gradually. Compared to after one inflow, the transitions between the regimes happens further up the inner part of the sill (figure 5.24 and 5.23). This may suggest that the velocity of the flow is slowed down earlier, due to denser water in the basin. Note that the estimate of the Froude number is a rough estimate, due to low resolution near the sill surface.

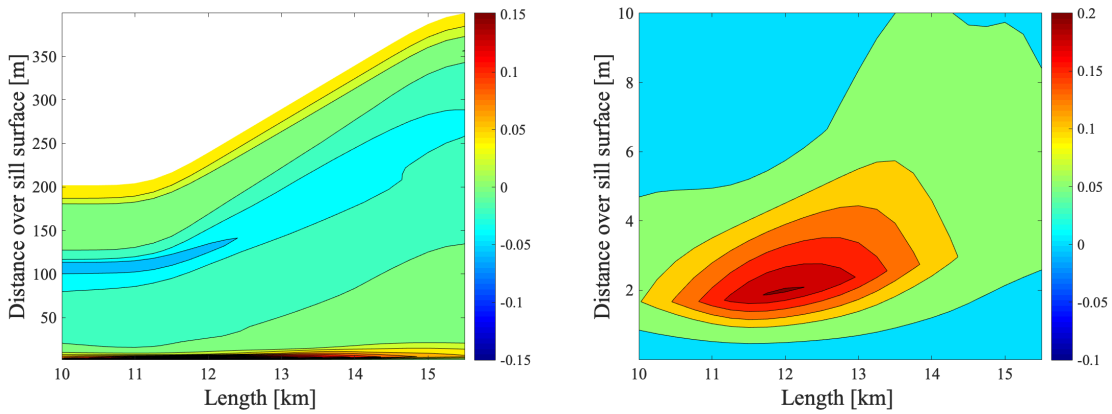

Figure 5.23: Profiles of the horizontal velocity, U [m s^{-1}], down the inner part of the sill. In (a) the entire depth above the sill is plotted, while only the lower 10 meters are plotted in (b).

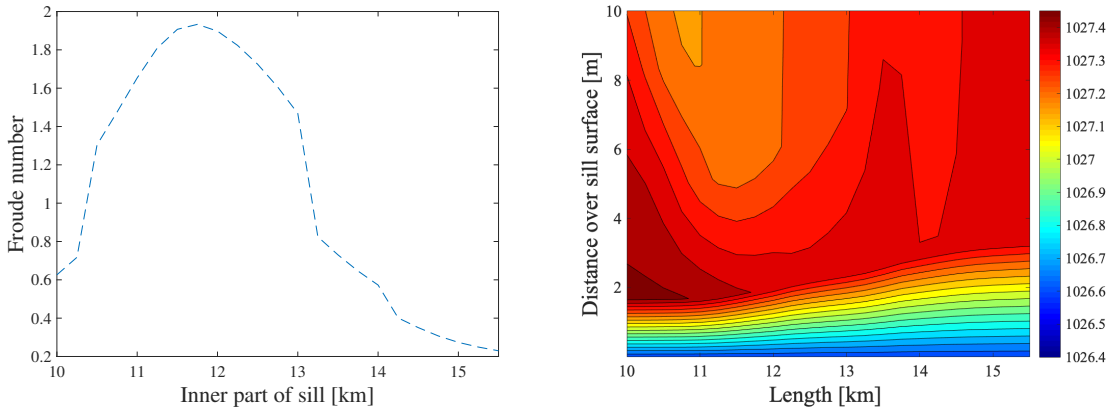

(a) (b)

Figure 5.24: A rough estimate of the Froude number (4.16), down the inner part of the sill, is plotted in (a), while a contour plot of the density, ρ [kg m^{-3}], in the lower 10 meters above the sill is plotted in (b).

The vertical velocity profile

The pattern of the vertical velocity at position II on the sill during the last four inflows are similar (figure 5.14d and 5.25). Negative velocities around 75-260 meters depth indicate transport of water down towards the fjord basin. The negative velocities are weakened during the last inflows, as the density gradient becomes weaker. The period of the tidal force, are visible in the contour lines, hence moving water up and down the sill. Small movements in the vertical velcity are also visible, due to disturbances in the density contours behind the sill (figure 5.19).

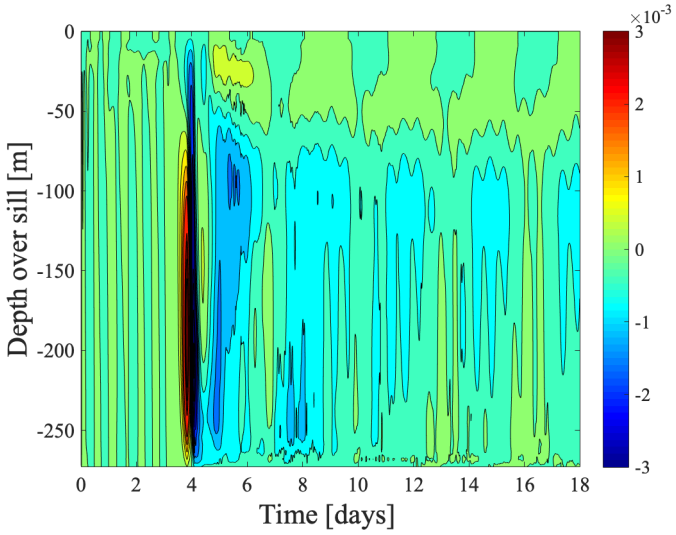

Figure 5.25: Time series of the vertical velocity, W [m s^{-1}], at position II at the sill (figure 5.14d). During the first 3 days only tidal force is present, thereafter five inflows of coastal water occur. The position is located approximately 2.75 kilometers from the sill top.

Contours of the passive tracers

Compared to after 1 coastal inflow, a further ascend of the oxygen-depleted marked bottom water is observed (figure 5.26). Additional dense water moving down towards the bottom of the basin, has resulted in this uplift. Parts of the ascended oxygen-depleted marked bottom water may be transported out of the fjor, e.g. due to tidal force, while the rest stabilizes around the sill level. Due to velocities over the sill, down the inner part of the fjord, a transport of marked bottom water back into the basin is observed near the sill surface (figure 5.26b). This explains the increase of RF during the last two inflows, as seen in figure 5.18.

A further transport of coastal water into the inner part of the fjord is observed (figure 5.27a). The coastal water is mainly transported over the sill and by the flow induced by the density gradient in the upper 100 meters. The

weakening of this flow during the inflows, due to mixing of fjord and coastal water are visible (figure 5.27b). As expected, the case of no coastal warming corresponds to a situation of almost complete basin exchange.

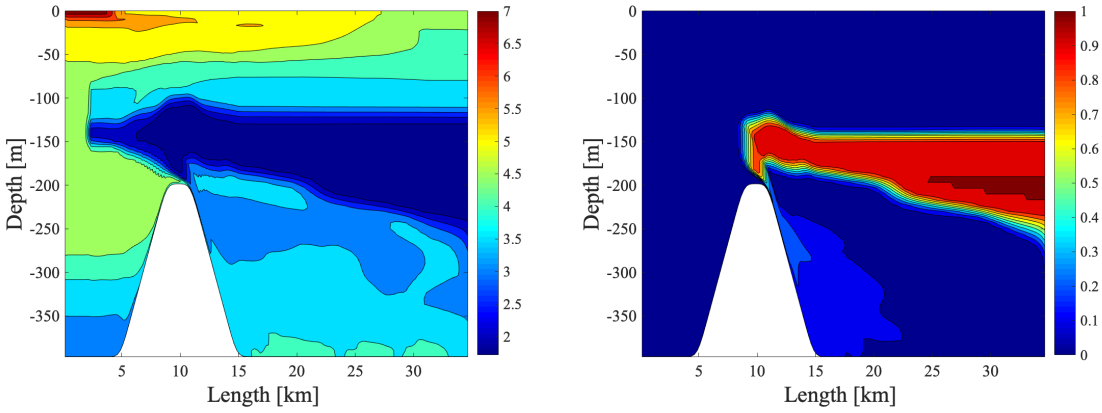

(a) (b)

Figure 5.26: Contour plots of (a) the O_2-tracer, marking the oxygen [ml l^{-1}], and (b) the θ-tracer, marking the bottom water in the fjord, after five inflows.

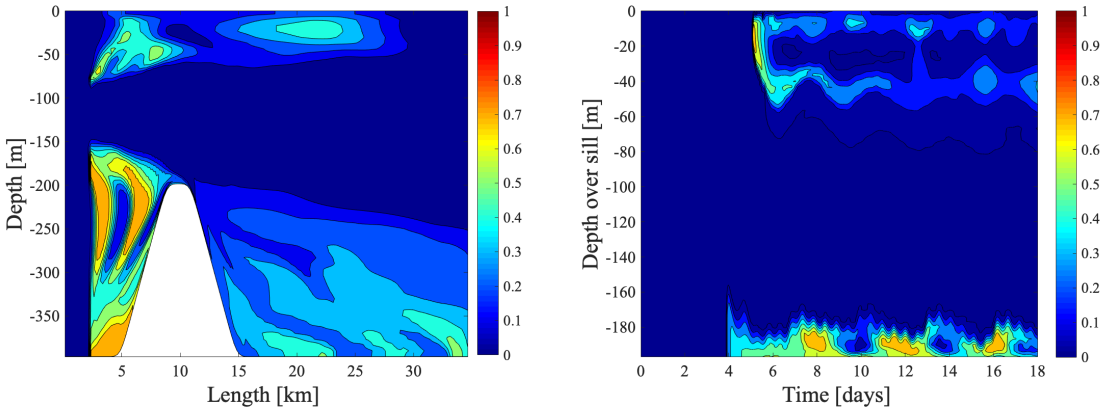

(a) (b)

Figure 5.27: Contour plots of the the ξ-tracer, marking the the coastal water. Figure (a) shows the profile after five inflows, while (b) shows a time series above the sill. During the first 3 days only tidal force is present, thereafter five inflows of coastal water occur.

The vertical eddy viscosity and Richardson number

During events of mixing and turbulence, values of the vertical eddy viscosity (K_M) typically ranges from $\mathcal{O}(10^{-3})$ to $\mathcal{O}(1)$. Water first moving over the sill top results in mixing of the water already situated near the sill surface. Consequently, an area with values of K_M signifying mixing is visible in the lower 20 meters above the sill surface around day 4 (figure 5.28a). Areas with large values of K_M around 120-180 meters depth are observed during day 5-18.

Figure 5.28b illustrates the value of the Richardson number (2.27) after 5 coastal inflows. Areas where the Richardson number is smaller than the critical Richardson value is marked in red, while areas where $Ri > Ri_c$ is marked in green. The critical Richardson number is set to $Ri_c = 0.25$. Accordingly, red regions indicate areas that are turbulent, or unstable. Stratification and vertical shear affect the production of turbulent kinetic energy. Strong stratification and weak vertical shear cause less turbulence, while weak stratification and strong vertical shear makes the fluid more receptive to turbulence. When dense water moves into the model area towards the sill, water situated outside the sill will be pushed towards it, resulting in mixing and dense water located over less dense water, hence unstability. Red areas above the sill are probably due to mixing as water moves over the sill, and the areas behind the sill and in the fjord basin may be results of the disturbances in the density isopycnals behind the sill (figure 5.19). Small density changes in the fjord basin, as observed in figure 5.20, makes the fluid more receptive to mixing and turbulence.

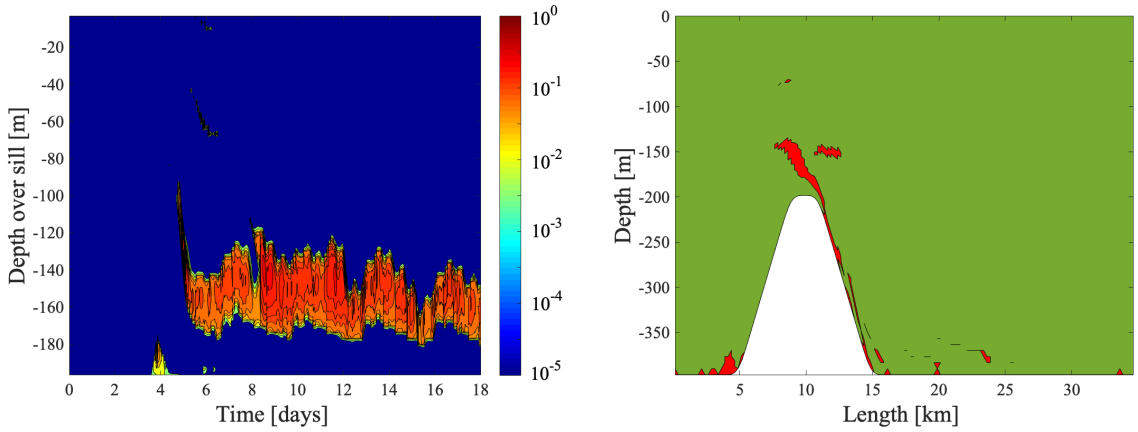

(a) (b)

Figure 5.28: Contour plots of (a) a time series of the vertical eddy viscosity, K_M [m^2 s^{-1}], above the sill, and (b) the Richardson number. Grid cells where $Ri < Ri_c$ are highlighted with red color, while areas where $Ri > Ri_c$ are highlighted with green. The critical Richardson number is set to $Ri_c = 0.25$.

5.3 Case 2: Coastal Warming of 1°C

After 5 Inflows of Coastal Water

Evolution of the marked bottom water

Two periods of decay of the remaining fraction of marked bottom water (RF) is observed during the first inflow (figure 5.29). The first period starts around day 4, lasting for about 18 hours. There is an increase for around 6 hours, before the second period starts around day 5. This period last until the second inflow starts at day 6, and is weaker than the first period.

The first period of decay is strong and appears to be a result of the interference between the tidal force and the coastal inflow. When the two forces is around the same phase, they strengthen each other. Some time later, they arrive out of phase, resulting in a short period of increase. The second period of decay is weaker than the first; hence the tidal force and the coastal inflow appear to be moving around the same phase, but to a smaller extent than the first period of decay.

There is a small period of decrease during the first hours into the second inflow, before the decay of RF stops, and then stars to decrease again between day 7 and 8. The next three inflows follow the same pattern; the decline of RF slows down at first, but around the middle of the inflow, it starts to increase, until the next inflow. During the last three inflows, the decay has a oscillating form, corresponding to each of the inflows. The period of the tidal force is visible in these oscillations.

After two coastal inflows, 15.2 % of the marked bottom water has been replaced by ambient water. After five inflows, 35.5 % has been replaced. This is a drastic worsening compared to 92.7 % in the case of no coastal warming, after 5 inflows.

The period of the tidal force is more visible in the evolution of RF compared to the case of no coastal warming. Hence, the tidal force seems to be more dominant, the strength of the coastal inflows weaker, or both.

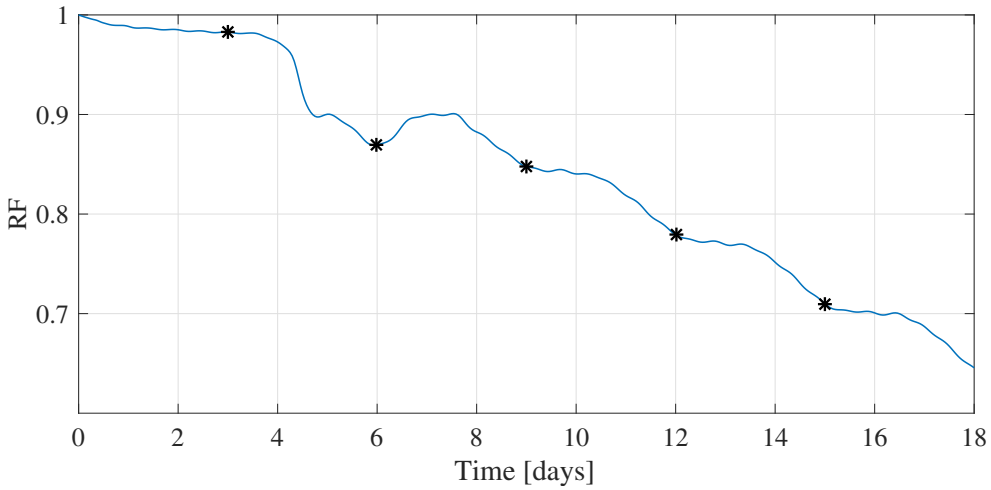

Figure 5.29: The remaining fraction of the marked bottom water (RF) plotted against time, during 3 days of tidal force and thereafter five coastal inflows. The starting time of an inflow is marked with a star ("*").

The density profile

Similar to the case of no coastal warming, there is a build up of dense water outside the sill (figure 5.30). A small increase in density is also visible in the middle of the fjord basin. However, the density increase outside the sill and in the fjord basin are considerable smaller compared to the case of no coastal warming (figure 5.31). Near the bottom of the basin there are areas of density decrease (figure 5.31b). Water flowing down the inner part of the sill towards the bottom of the basin push water situated in the basin down and towards the eastern boundary, due to having momentum. Thus, dense water near the bottom of the basin is replaced by less dense water descending from the top of the sill. This may explain the density decrease near the bottom.

This was not seen in the previous case, as denser water was flowing over the sill and into the basin, resulting in a density increase instead of decrease.

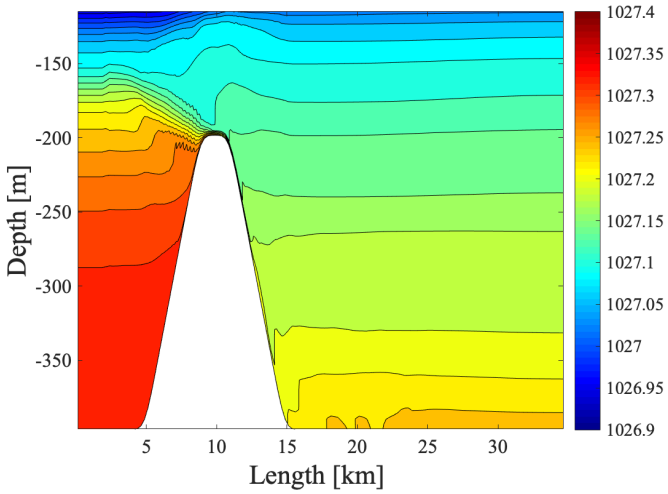

Figure 5.30: Contour plots of the density, ρ [kg m^{-3}], after five coastal inflows. Only the lower 285 meters are plotted as the area around the sill is of interest.

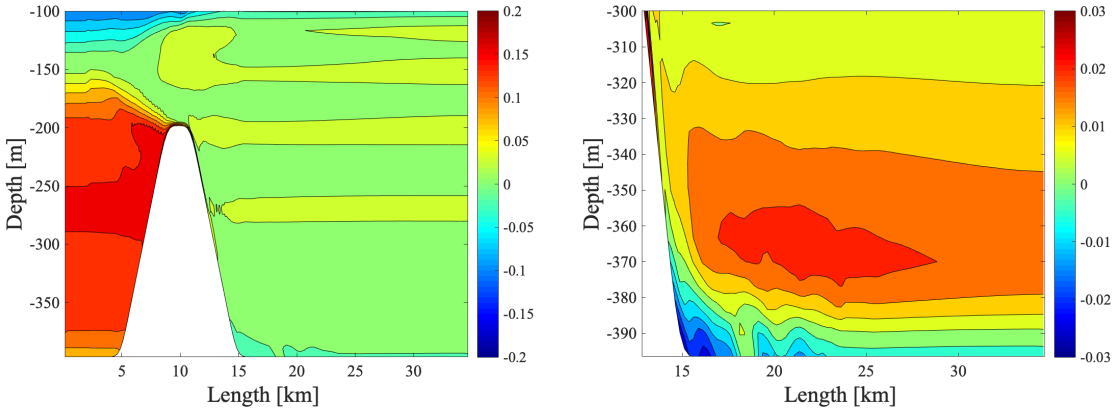

(a) (b)

Figure 5.31: Contour plots of the change in density after five coastal inflows compared to after 3 days of only tidal force, $\Delta\rho_5$ [kg m^{-3}]. Only the lower 300 meters of the model area is plotted in (a), as the area near the sill surface is of interest. The lower 100 meters of the fjord basin is plotted in (b).

As in the case of no coastal warming, there is a density increase above the sill during the first inflow (figure 5.32). However, the increase is weaker and only occurs in the lower 80 meters above the sill. This is reasonable since the build up of dense water outside the sill is less dense, as noted in figure 5.31a. The inflows of dense water near the surface of the sill are considerable weaker, hence less dense water are transported into the fjord basin. The oscillating pattern, caused by the tidal force, is still observed in the density contours.

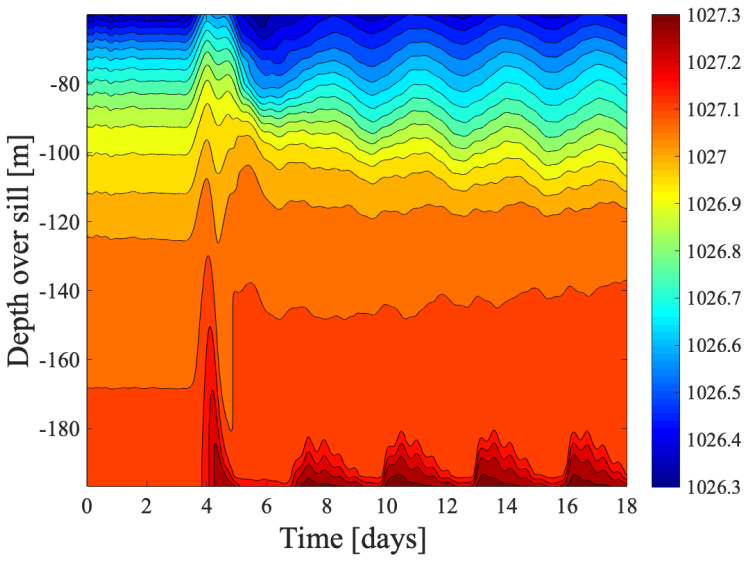

Figure 5.32: Time series of the density, ρ [kg m^{-3}], above the sill. During the first 3 days only tidal force is present, thereafter five inflows of coastal water occur. Only the lower 140 meters are plotted as the area near the sill surface is of interest.

The horizontal velocity profile

The horizontal velocitiy near the sill surface during the first inflow is significantly lower than in the case of no coastal warming (figure 5.33). Consequently, the compensating negative velocitiy near the water surface is also lower. This may be explained by weaker density gradients between the fjord and coastal water, hence weaker flows generated by these gradients (figure 4.11). The flow of dense water near the sill surface is weaker during the last four inflows, suggesting less transport of water into the basin.

The velocity induced by the density gradient between the fjord and coastal water, at 5-60 meters depth around day 5-6, is some weaker during the first inflow. However, it is approximately the same velocity as in the case of no coastal warming during the next four inflows. The compensating negative velocities around 70-190 meters depth are also weaker during the inflows. As in the previous case, the period of the tidal force is visible in the velocity contours.

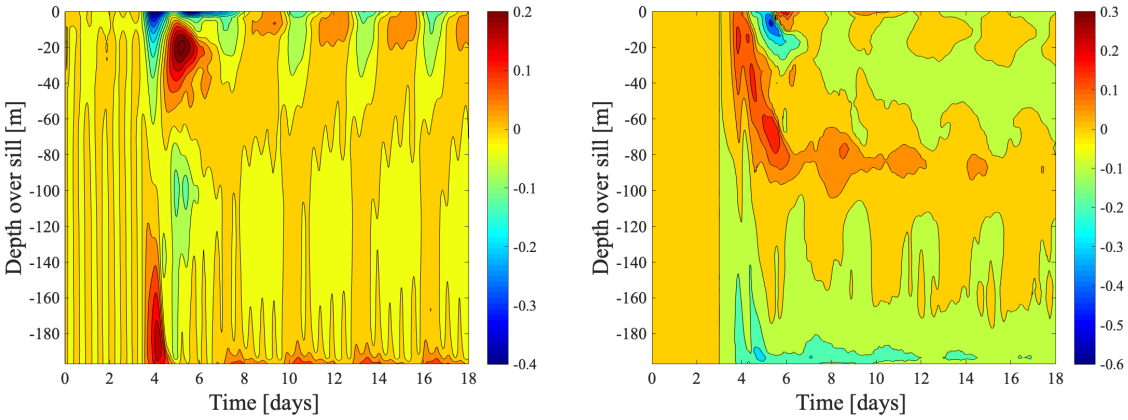

(a) (b)

Figure 5.33: Time series of (a) the horizontal velocity, U [m s^{-1}], above the sill. During the first 3 days only tidal force is present, thereafter five inflows of coastal water occur. Figure (b) shows the change in horizontal velocity compared to the case of no coastal warming.

Estimates of the Froude number suggests a transition from subcritical to supercritical flow around one and a half kilometers from the sill top, down the inner part of the sill (figure 5.35a). This is slightly further down the sill, compared to the case of no coastal warming. A transition from a supercritical to a subcritical regime happens earlier than in the case of no coastal warming, around two kilometers from the sill top. This is reasonable, as the velocity over the sill and down the inner part of the sill is lower in this case (figure 5.34b). The increase of the plume height (h'), due to conserve mass (5.2), is similar to the case of no coastal warming (figure 5.34). Note that the estimate of the Froude number is a rough estimate, due to low resolution near the sill surface.

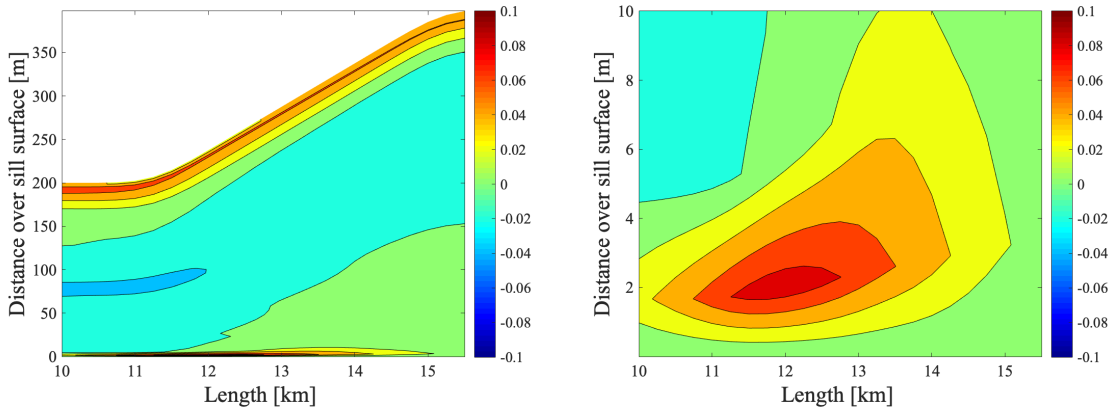

Figure 5.34: Profiles of the horizontal velocity, U [m s^{-1}], down the inner part of the sill. In (a) the entire depth above the sill is plotted, while only the lower 10 meters are plotted in (b).

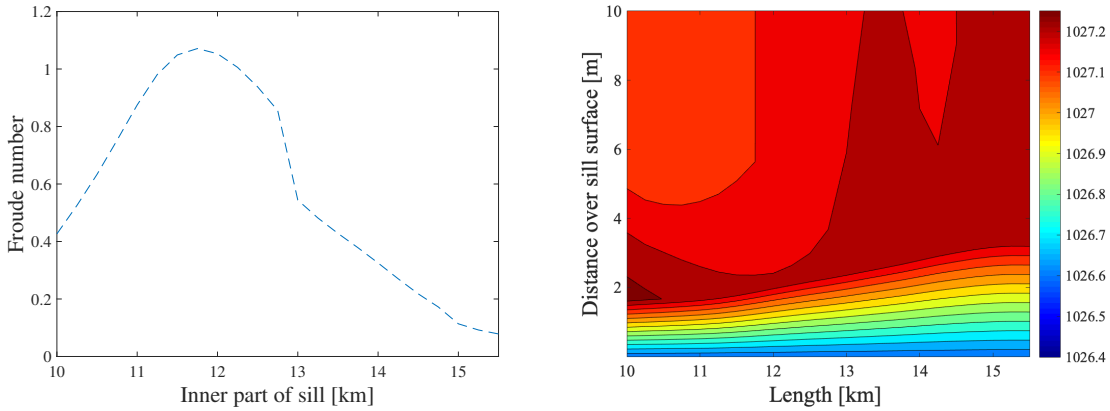

(a) (b)

Figure 5.35: A rough estimate of the Froude number (4.16), down the inner part of the sill, is plotted in (a), while a contour plot of the density, ρ [kg m^{-3}], in the lower 10 meters above the sill is plotted in (b).

The vertical velocity profile

As also observed in the case with no coastal warming, a positive vertical velocity followed by a negative velocity is visible around 24 hours into the first inflow, at position II on the sill (figure 5.14d). However, the vertical velocities are now weaker (figure 5.36). During the next four inflows, the negative vertical velocity has approximately the same strength, but covers a smaller depth and lasts for a smaller extend of time. As in the previous case, the period of the tidal force is visible in the contour lines, thus the tide moves water up and down the sill. In this case, fewer small movements is visible in the time series, indicating that the oscillations in the density contours at the position is fewer. This compares well with the density profile in figure 5.30.

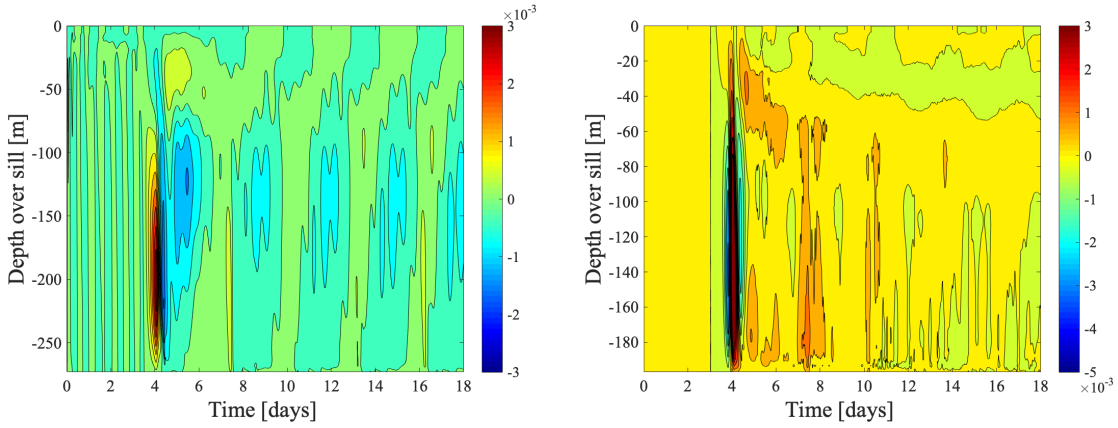

(a) (b)

Figure 5.36: Time series of (a) the vertical velocity, W [m s^{-1}], at position II at the sill (figure 5.14d). During the first 3 days only tidal force is present, thereafter five inflows of coastal water occur. Figure (b) shows the change in vertical velocity compared to the case of no coastal warming. The position is located approximately 2.75 kilometers from the sill top.

Contours of the passive tracers

Similary to the case of no coastal warming, water flowing over the sill has intruded into the basin water, and down to the bottom (figure 5.37 and 5.38a). However, the water has only moved around half way towards the eastern boundary, causing a small ascend of the marked bottom water. This is a considerable difference compared to the case of no coastal warming, where the water reached the eastern boundary, filling almost the entire basin. As also observed in the previous case, the transport of coastal water near the water surface, induced by the density gradient between the fjord and coastal water, becomes weaker after the second inflow (figure 5.38a-b). This may be caused by a slower decrease of the density gradient.

Warming of the coastal water cause a density reduction, making the oceanic source water less heavy. Before conducting the numerical simulations, a

effect on the water exchange was expected. However, the results from the numerical simulations in this case suggests a surprisingly strong effect of coastal warming on the basin exchange.

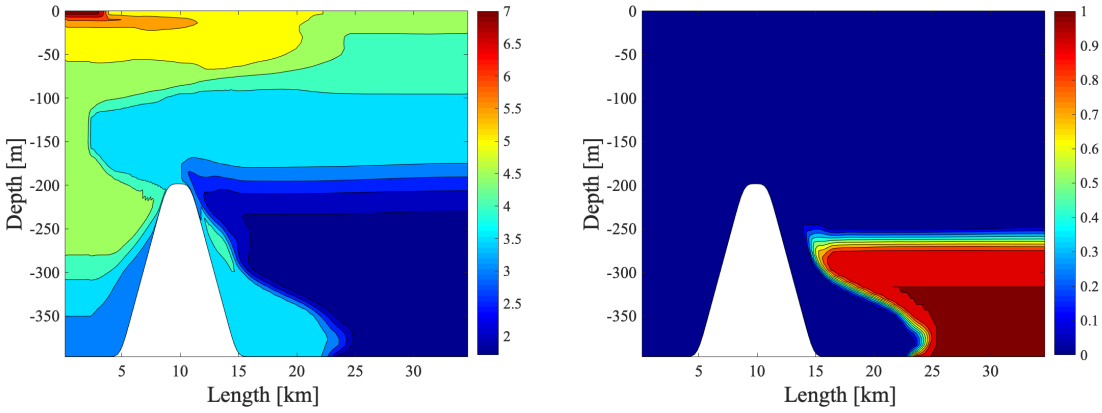

(a) (b)

Figure 5.37: Contour plots of (a) the O_2-tracer, marking the oxygen [ml l^{-1}], and (b) the θ-tracer, marking the bottom water in the fjord, after five inflows.

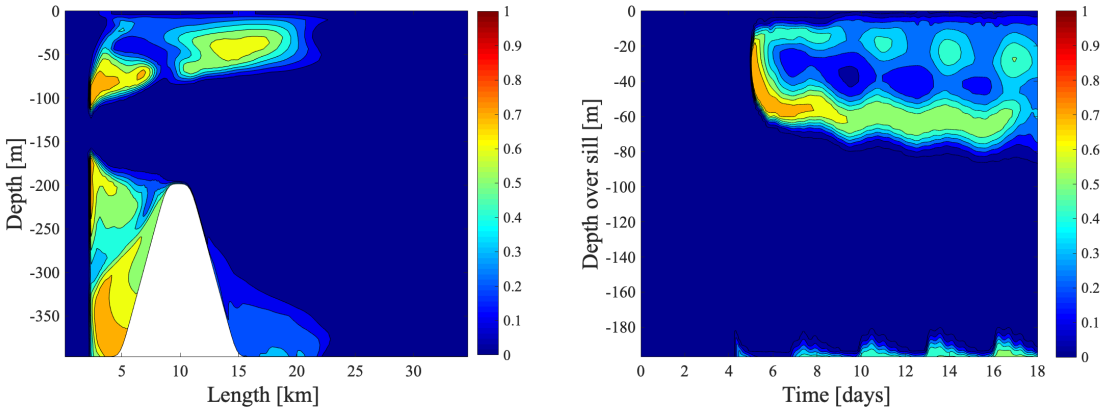

(a) (b)

Figure 5.38: Contour plots of the the ξ-tracer, marking the coastal water. Figure (a) shows the profile after five inflows, while (b) shows a time series above the sill. During the first 3 days only tidal force is present, thereafter five inflows of coastal water occur.

The vertical eddy viscosity and Richardson number

Areas with values of K_M signifying turbulence are observed in the lower 60 meters above the sill surface (figure 5.28a). These are probably a result of mixing when water moves over the sill during inflows. The areas are smaller than in the case of no coastal warming.

Compared to the previous case, there are fewer areas with Richardson number smaller than the critical Richardson number. This is consistent with the density profile, as the disturbances in the density isopycnals behind the sill are smaller than in the case of no coastal warming (figure 5.30). However, areas of turbulence are still visible above the sill and close to the inner part of the sill, near the basin (figure 5.39b). The small density changes observed in the fjord basin (figure 5.31) makes the fluid more receptive to mixing and turbulence. Particularly the areas with density decrease close to the basin bottom, near the lower part of the sill, as seen in figure 5.31.

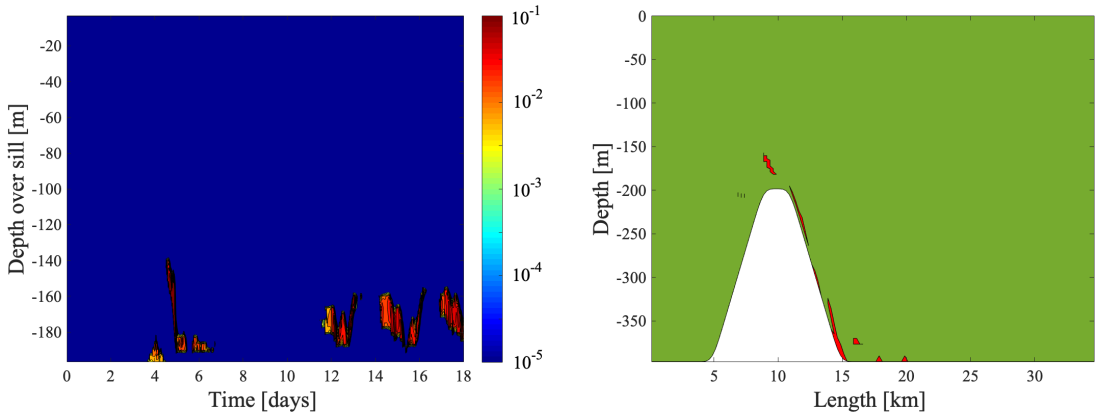

Figure 5.39: Contour plots of (a) a time series of the vertical eddy viscosity, K_M [m^2 s^{-1}], above the sill, and (b) the Richardson number. Grid cells where $Ri < Ri_c$ are highlighted with red color, while areas where $Ri > Ri_c$ are highlighted with green. The critical Richardson number is set to $Ri_c = 0.25$.

5.4 Case 2: Coastal Warming of 2°C

After 5 Inflows of Coastal Water

Evolution of the marked bottom water

During the first inflow there are two periods of decay of the remaining fraction of marked bottom water (RF) (figure 5.40). The first period starts around day 4, lasting for about 20 hours. A small period of strong increase follows, before the second decay starts around 53 hours into the first inflow. The two periods of strong decay and increase are probably results of the interaction between the external forces; the tide and the coastal inflow. When interacting, the two forces will weaken or intensify each other, resulting in a strong increase or decrease of RF. During the next four inflows, this interaction is visible. The tidal period can be seen during the inflows together with periods of increase or decrease of RF.

Compared to the cases with no coastal warming and coastal warming of 1°C, the tidal force appears to be more dominant in this case. Warming of the coastal water cause a density reduction, resulting in weaker density gradients between the fjord and coastal water. This may explain why the tidal force appears more dominant. As seen in the base case, the tidal force is moving the bottom water up and down, but do not influence the exchange of the lower basin water.

After two coastal inflows, 3.1 % of the marked bottom water has been replaced by ambient water. After five coastal inflows, 3.7 % has been replaced. This is a dramatic worsening compared to the two previous main cases, especially the case of no coastal warming where 92.8 % was replaced, after five inflows.

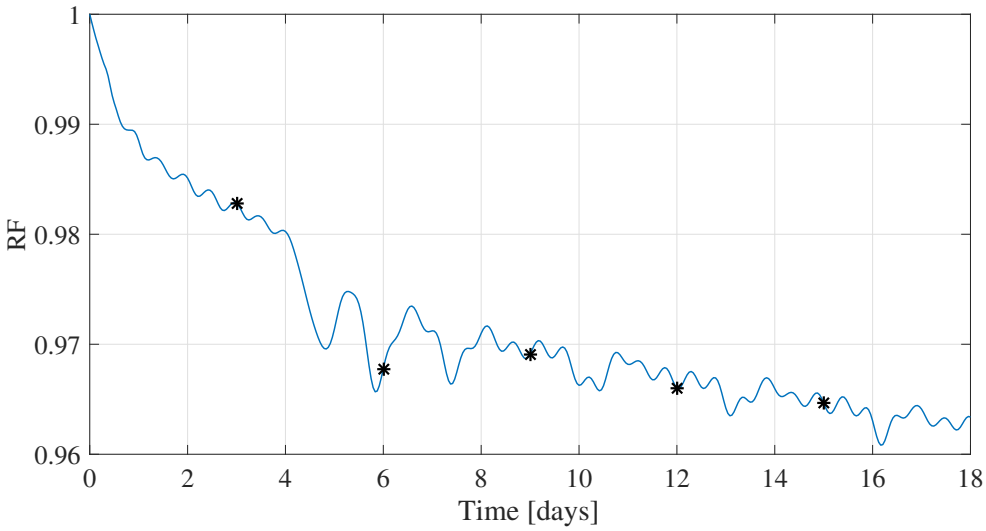

Figure 5.40: The remaining fraction of the marked bottom water (RF) plotted against time, during 3 days of tidal force and thereafter five coastal inflows. The starting time of an inflow is marked with a star ("*").

The density profile

There are no build up of dense water outside the sill (figure 5.41). The density contours are close to horizontally homogeneous, with some disturbances near the sill. This is a significant difference in comparison to the two previous main cases, where a build up of dense water was observed outside the sill. Apart from some areas with small density increase or no change (dark orange areas in figure 5.42a), there are only regions of density decrease in the lower 100 meters of the model area.

As in the case of 1°C of coastal warming, there is a thin layer of density decrease at the bottom of the fjord basin (figure 5.42b). However, this change is considerably smaller than in the previous case. This may be caused by water flowing down the lower inner part of the sill, pushing water situated near the bottom below its equilibrium level, and hence resulting in small

decreases in density.

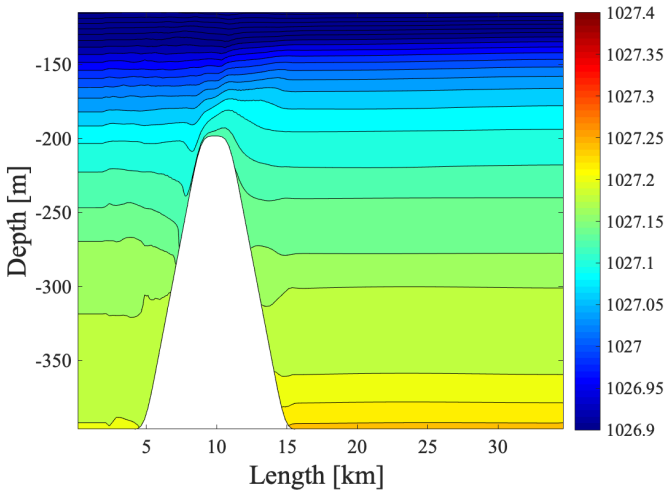

Figure 5.41: Contour plots of the density, ρ [kg m^{-3}], after five coastal inflows. Only the lower 285 meters are plotted as the area around the sill is of interest.

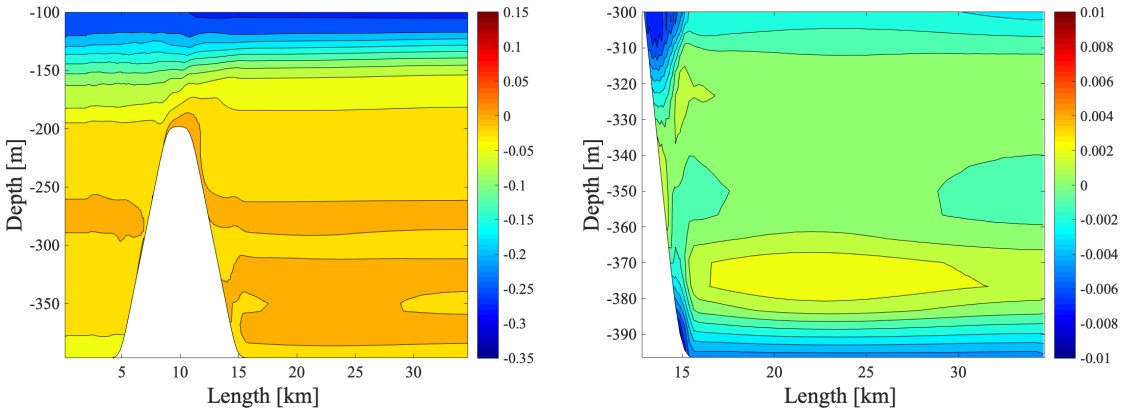

Figure 5.42: Contour plots of the change in density after five coastal inflows compared to after 3 days of only tidal force, $\Delta\rho_5$ [kg m^{-3}]. Only the lower 300 meters of the model area is plotted in (a), as the area near the sill surface is of interest. The lower 100 meters of the fjord basin is plotted in (b).

Around 12 hours into the first coastal inflow there is a decline in the density profile in the lower 140 meters above the sill (figure 5.43). In contrast to the two previous main cases, this suggests flows of less dense water over the sill. This may be caused by flows due to conservation of volume, or flows generated by the density gradient. Initially, the coastal water is less dense than the fjord water in the lower 120 meters above the sill surface (figure 4.11). However, the density profiles may change in the model area and in time.

As also observed in the cases of no coastal warming and 1°C of coastal warming, oscillating patterns in the density contours, corresponding to the last four coastal inflows and the period of the tide, is visible during day 7-18.

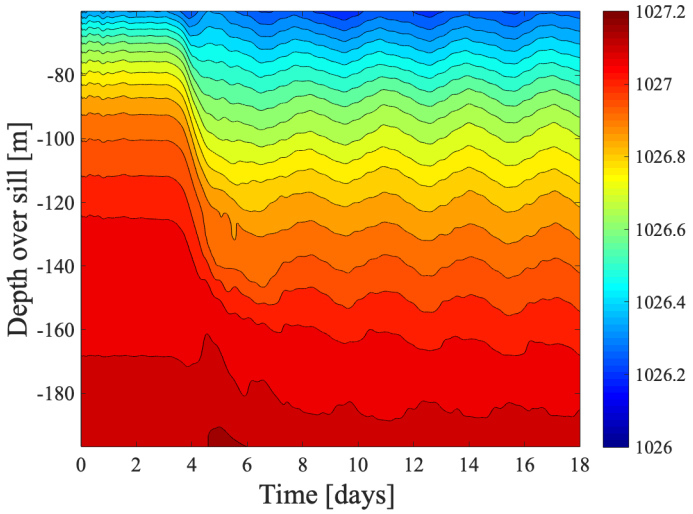

Figure 5.43: Time series of the density, ρ [kg m^{-3}], above the sill. During the first 3 days only tidal force is present, thereafter five inflows of coastal water occur.

The horizontal velocity profile

Initially, there is a negative density gradient ($\frac{\partial \rho}{\partial x} < 0$) in the upper 60 meters, and a smaller positive density gradient ($\frac{\partial \rho}{\partial x} > 0$) in the lower 140 meters above the sill, between the fjord and coastal water (figure 4.11). To balance out these negative and positive gradients, positive and negative flows are generated, respectively. As in the two previous cases, a positive velocity generated by the negative density gradient is observed around day 4 (figure 5.44). Due to conservation of volume, a compensating negative velocity is visible near the water surface. A negative velocity is also observed in the lower 80 meters. This is probably generated to conserve volume, but may also be caused by the positive density gradient. During the last four inflows, this velocity is reduced, to approximately the same magnitude as in the case of no coastal warming. A decrease of the density contours above the sill was observed in figure 5.43, after the first inflow. The decrease near the sill surface is probably due to water of less density moving out of the fjord basin. This is consistent with the horizontal velocity at the inner part of the sill in figure 5.45. This may also explain the region of largest density decrease around 100-180 meters depth in figure 5.42a.

Compared to the two previous main cases, there are no apparent positive velocities near the sill surface during the inflows (figure 5.44). This is probably a result of a weaker density gradient between the fjord and coastal water near the sill.

In contrast to the two previous main cases, the horizontal velocity down the inner part of the sill is negative, transporting water out of the fjord basin (figure 5.45). As there is no gravity plume down the sill, discussion of the Froude number (4.16) and possible hydraulic jumps are not relevant.

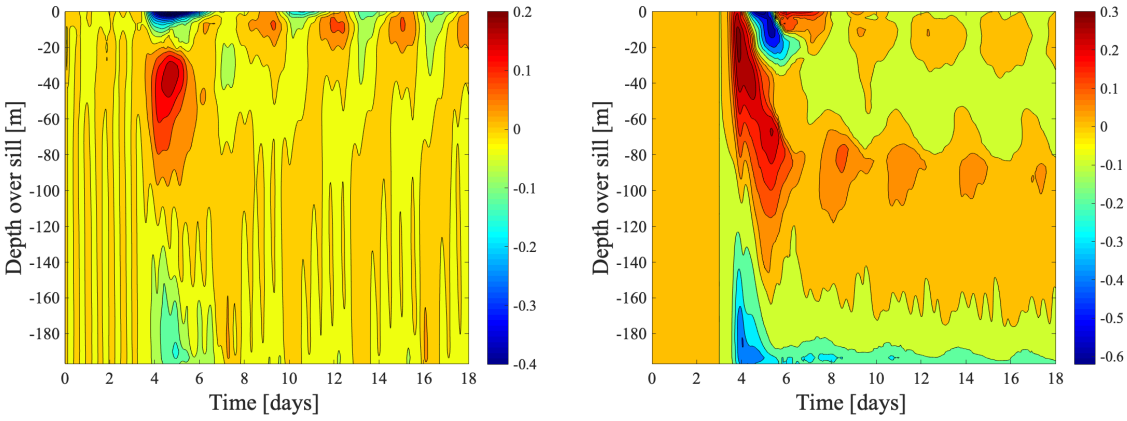

(a) (b)

Figure 5.44: Time series of (a) the horizontal velocity, U [m s^{-1}], above the sill. During the first 3 days only tidal force is present, thereafter five inflows of coastal water occur. Figure (b) shows the change in horizontal velocity compared to th case of no coastal warming.

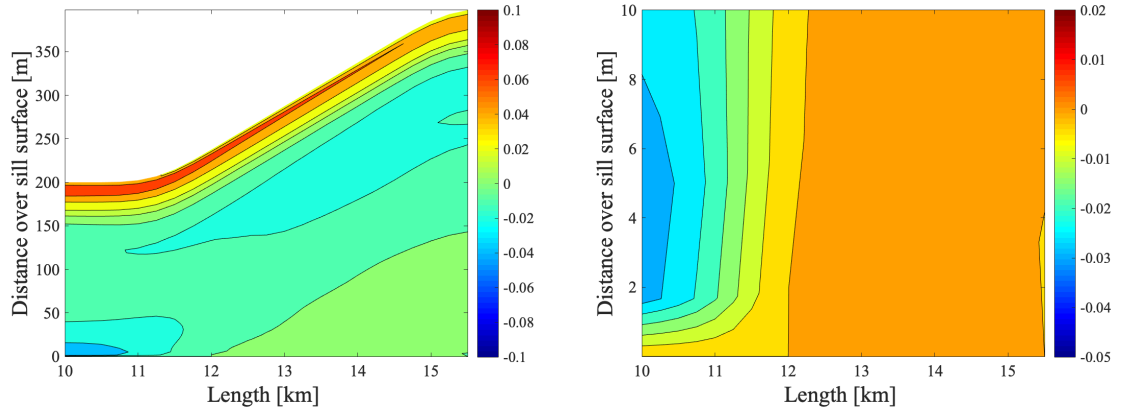

(a) (b)

Figure 5.45: Profiles of the horizontal velocity, U [m s^{-1}], down the inner part of the sill. In (a) the entire depth above the sill is plotted, while only the lower 10 meters are plotted in (b).

The vertical velocity profile

Around 24 hours into the first inflow, a positive vertical velocity is visible in the upper 20-100 meters at position II on the sill (figure 5.14d and 5.46a). During the same time period a negative velocity can be seen around 120-250 meters depth. This is unlike the previous main cases, where a positive vertical velocity was followed by a negative velocity around day 4. This is apparently a result of the density gradients (figure 4.11). The velocities are considerable weaker than in the two previous main cases, and lasts for a longer period of time, around 48 hours.

During the next four inflows the negative vertical velocity is weaker than in the previous cases, and the positive vertical velocities, between the inflows, are larger (figure 5.46b). This signify less transport of water into the basin. Fewer small movements are observed in the velocity profile, indicating that the disturbance in the density contours behind the sill is fewer. This is consistent with figure 5.41.

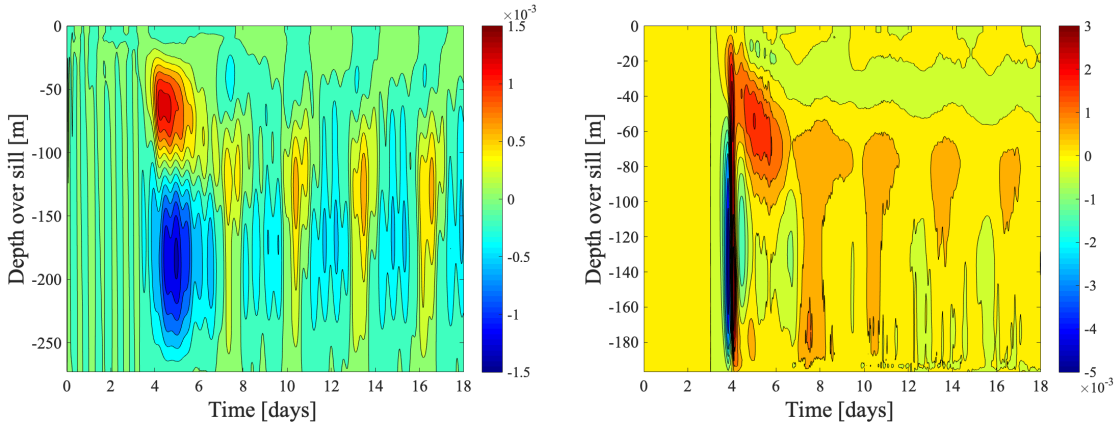

(a) (b)

Figure 5.46: Time series of (a) the vertical velocity, W [m s^{-1}], at position II at the sill (figure 5.14d). During the first 3 days only tidal force is present, thereafter five inflows of coastal water occur. Figure (b) shows the change in vertical velocity compared to the case of no coastal warming. The position is located approximately 2.75 kilometers from the sill top. Remark: the contour levels in (a) are different from equivalent plots in the previous cases.

Contours of the passive tracers

The oxygen profile of the basin area is similar to the profile after 3 days of only tidal force (figure 5.2a and 5.47a). Due to negative horizontal velocities up the inner part of the sill, some oxygen-depleted water has been transported from the basin to the outer part of the fjord. However, this transport is minor. The contour profile of the marked bottom water is also similar to the profile after 3 days with only tidal force (figure 5.2b and 5.47b). A minor ascend of the bottom water may be observed. No coastal water has moved over the sill surface and into the basin water (figure 5.38). This is a significant change compared to the previous cases.

The only transport of coastal water into the inner part of the fjord occur in the upper 120 meters (figure 5.38b). The area of transport is considerably

larger than in the previous cases. The positive velocity, generate by the density gradient, covers a larger depth during the first inflow (figure 5.44). This may explain the increased transport. Weaker negative velocities around 70-100 meters depth during the inflows may also contribute.

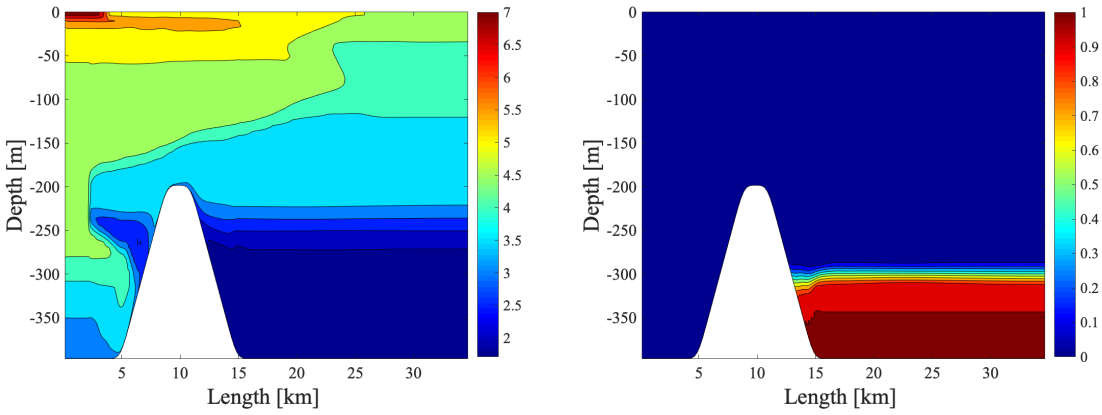

Figure 5.47: Contour plots of (a) the O_2-tracer, marking the oxygen [ml l^{-1}], and (b) the θ-tracer, marking the bottom water in the fjord, after five coastal inflows.

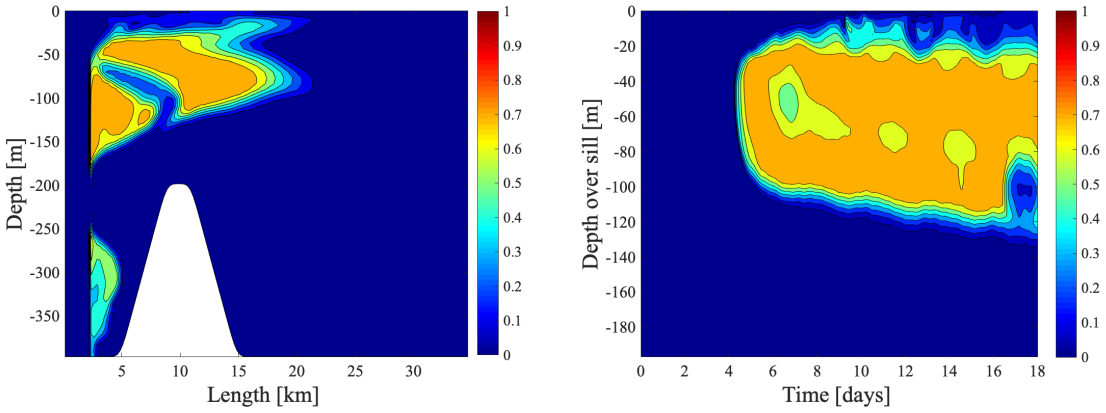

(a) (b)

Figure 5.48: Contour plots of the the ξ-tracer, marking the the coastal water. Figure (a) shows the profile in the model area after five inflows, while (b) shows a time series above the sill. During the first 3 days only tidal force is present, thereafter five inflows of coastal water occur.

The vertical eddy viscosity and Richardson number

Only two small areas with values of K_M signifying mixing and turbulence are visible in the model area (figure 5.49a). These are found around day 4-5 at 20 meters depth, and are probably results of the start-up of the flow induced by the density gradient between the coastal and fjord water. However, the overall size of the vertical eddy viscosity in signify that there are no dramatic turbulence or instability above the sill during the inflows.

No visible areas with Richardson number smaller than the critical Richardson number are observed (figure 5.49b). Hence, the model area is apparently stable with no visible regions of turbulence. Compared to the previous two main cases, the disturbances in the density isopycnals near the sill in the basin is fewer and less dramatic (figure 5.41). As seen in figure 5.41, the density profile of the model area is almost horizontally homogeneous, i.e. relatively stable. Stratification in the fluid contribute to less turbulence. This stable

model area is a significant difference compared to the two previous main cases, especially the case of no coastal warming.

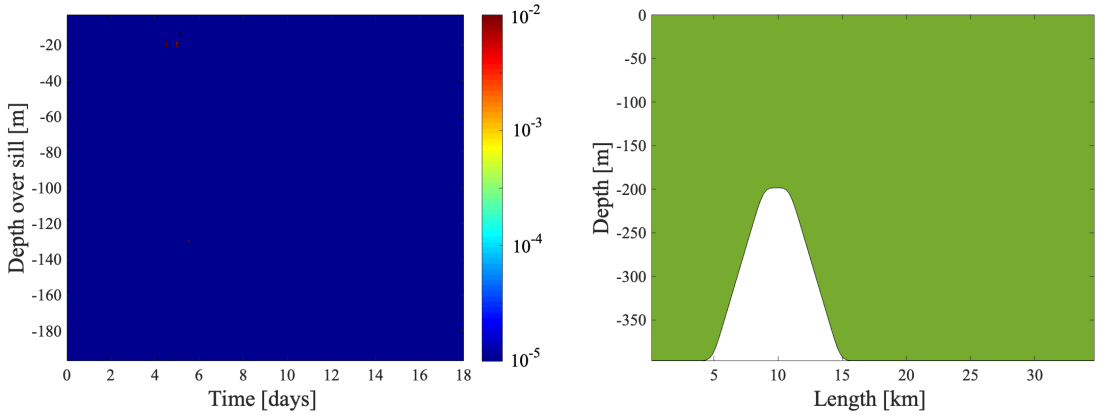

(a) (b)

Figure 5.49: Contour plots of (a) a time series of the vertical eddy viscosity, K_M [m^2 s^{-1}], above the sill, and (b) the Richardson number. Grid cells where $Ri < Ri_c$ are highlighted with red color, while areas where $Ri > Ri_c$ are highlighted with green. The critical Richardson number is set to $Ri_c = 0.25$..

Chapter 6

Summary and Conclusions

In this thesis, the effect of coastal warming on the water exchange in sill fjords has been investigated. A three-dimensional hydrostatic ocean model, the Bergen Ocean Model, has been applied to simulate inflows from the coast into a sill fjord. An idealized fjord topography, resembling Sørfjorden, located outside Bergen, was used as the model area. The lower 100 meters of the basin water was marked, and two main cases were investigated; without and with coastal warming. For the case of coastal warming, 1°C and 2°C warming were investigated.

With no coastal warming, 88 % of the marked bottom water was replaced by ambient water, after two coastal inflows. For the cases with 1°C and 2°C of coastal warming, only 15 % and 3% was replaced. After five coastal inflows, the percentage of replaced marked bottom water was 92%, 35%, and 3%, respectively. The results indicate that a warming of 1°C of the coastal water has a major effect on the amount of water exchanged in the sill fjord. A 2°C warming results in a further decrease of the basin exchange. Accordingly, the results indicate that events of almost full basin exchange, as the case of no coastal warming represented, will occur less frequently due to warming of the coastal water.

The results suggests that the observed warming of the oceanic source water during the last four decades has resulted in less frequent events of exchange of the lower basin water in sill fjords like Sørfjorden. Less frequent events of lower basin exchange, may result in a reduced ventilation of the oxygen-depleted basin water. This was supported by the oxygen profiles obtained in the numerical simulations. With longer stagation periods, the water quality of the basin water may get worse due to e.g. biological consumption.

The indications from the results obtained in the present study support the findings of Aksnes *et al.* (2019) that the warming of the basin's oceanic source water results in less frequent events of exchange of the basin water. This results in deoxygenation, and thus worse water quality.

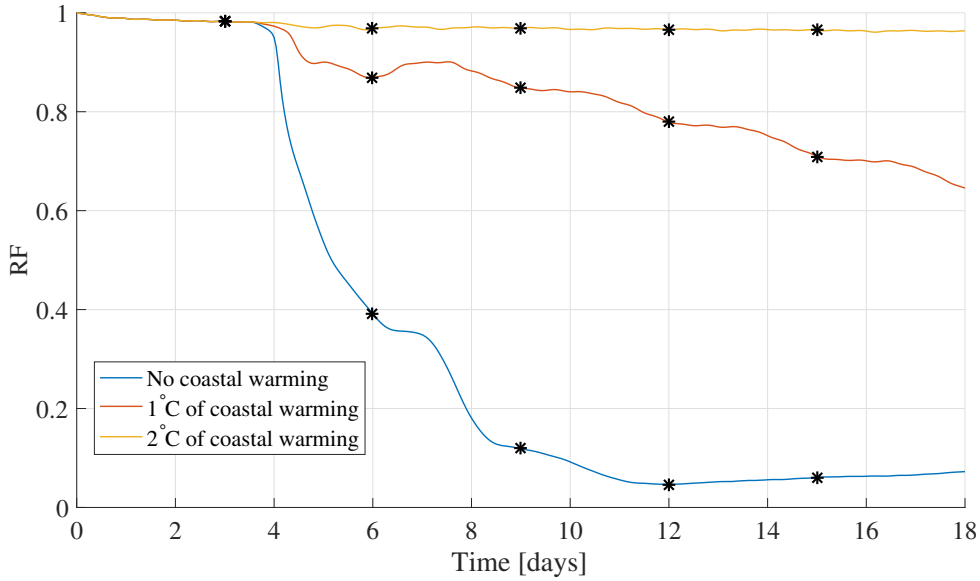

Figure 6.1: The remaining fraction of the marked bottom water (RF) plotted against time, during 3 days of tidal force and thereafter five coastal inflows. The starting time of an inflow is marked with a star ("*").

A further worsening of the water quality due to climate change will potentially have significant consequences for the fjord ecosystems and services, e.g. aquacultures. The deoxygenation of the basin water affects biodiversity and may reduce the holding capacity for fish farming in the fjords (Aksnes et al., 2019; Soltveit and Jensen, 2018).

Further Work

In the present study, several assumptions and simplifications were made, impacting the reliability of the results. In order to extend the results from this study, some further work will be mentioned.

The results in this thesis are dependent on the ocean model applied in the simulations. It should be checked that BOM successfully is able to reconstruct measured events of inflow from the coast.

For the purpose of this thesis, temperature and salinity profiles at the coastal hydrographic station Ytre Utsira was assumed to be representable for the oceanic source water of Sørfjorden. A theoretical exponential profile for the salinity was made and the temperature was set constant for all depths, both based on the profiles at Ytre Utsira. The temperature and salinity profile of the fjord water was based on hydrographic data from NORCE, averaged over seasonal times. In order to extend the results from this thesis, the profiles should be set to more exact profiles, representing typical situations of coastal inflow. Five coastal inflows was chosen. In further work this may be changed to represent a typical situation.

The main focus of the present study was the general dynamics in the fjord during inflows from the coast. In future work, the grid resolution could be improved, in order to resolve motions on smaller scales that were not represented with the present grid size. This would also result in more accurate

estimates of the Froude number (4.16). Only one sill and its associated basin was investigated. A more complex model area of the fjord topography would also improve the realism of the numerical results.

The horizontal eddy viscosity was in this study set to $A_M = 400$ m^{2}s^{-1}. The parameter was set large enough to avoid grid scale noises in the flow field, and small enough to allow the representation of the flow in and out of the fjord. As the overall water exchange in sill fjords was the main focus in this study, the parameter was set relatively large. Blumberg and Mellor (1987) state that values of A_M as low as 10 m^{2}s^{-1} have been applied successfully in various applications. Thus, in future work, it could be investigated if smaller values of A_M would affect the dynamics in the fjord during this study.

The Coriolis force was neglected due to the width of the fjord being smaller than the baroclinic Rossby radius of deformation. In future studies, the Coriolis force might be included in order to investigate possible effects of the force.

Possible actions to reduce the trend of deoxygenation, and to improve the water quality in the fjord basin have been proposed (Soltveit and Jensen, 2018; Sand, 2018). One of the suggested methods is to place a submerged freshwater discharge at the bottom of the basin to increase the circulation and ventilation of the basin water (Sand, 2018). Actions such as this could be used to compensate for reduced basin water renewal during a warming ocean scenario. Nevertheless, further knowledge about possible methods are needed.

The water quality in sill fjords are dependent on several factors. The exchange of water between the fjord and coastal waters was the focus of this thesis. In addition, the water quality is dependent on other factors, e.g. wind and fresh water supply (Sætre, 2007). However, these generally do not affect the lower basin water.

Appendix A

List of symbols

symbol	description	unit
U	Velocity component in x-direction	m s^{-1}
V	Velocity component in y-direction	m s^{-1}
W	Velocity component in z-direction	m s^{-1}
t	Time	s
ρ	Density	kg m^{-3}
ρ_0	Reference density	kg m^{-3}
ρ'	Density perturbation	kg m^{-3}
p	Pressure	Pa = kg m^{-1} s^{-2}
g	Gravitational acceleration (g ≈ 9.81)	m s^{-2}
μ	Viscosity	kg m^{-1} s^{-1}
f	The Coriolis parameter	rad s^{-1}
T	Temperature	°C
T_F	Temperature of the fjord water	°C
T_C	Temperature of the coastal water	°C
S	Salinity	psu
S_F	Salinity of the fjord water	psu
S_C	Salinity of the coastal water	psu
η	Surface elevation from $z = 0$	m
H	Bottom static depth	m
D	Bottom dynamic depth ($H + \eta$)	m

symbol	**description**	**unit**
A_M	Horizontal eddy viscosity	$m^2\ s^{-1}$
K_M	Vertical eddy viscosity	$m^2\ s^{-1}$
A_H	Horizontal eddy diffusivity	$m^2\ s^{-1}$
K_H	Vertical eddy diffusivity	$m^2\ s^{-1}$
O_2	Passive tracer marking the oxygen	$ml\ l^{-1}$
θ	Passive tracer marking the bottom water	
ξ	Passive tracer marking the coastal water	
β	Relaxation parameter in the FRS	
a	Amplitude of the relaxation parameter	
t_0	Starting time	s
T_p	Period of the coastal inflow	hours
T_{M_2}	Period of the main component of the tide (M_2)	hours
V_θ	Volume of remaining marked bottom water	m^3
V_0	Initial volume of remaining marked bottom water	m^3
RF	The remaining fraction of marked bottom water	

Symbols with blank space at unit are dimensionless numbers.

Bibliography

Aksnes, D. L., Aure, J., Johansen, P.-O., and Salvanes, A. G. V. (2019). Multi-decadal warming and associated decline in dissolved oxygen of deep fjord basins. In preparation.

Arakawa, A. (1966). Computational design for long-term numerical integration of the equations of fluid motion: Two-dimensional incompressible flow. part i. *Journal of computational physics*, 1(1):119–143.

Asplin, L., Salvanes, A. G. V., and Kristoffersen, J. B. (1999). Nonlocal wind-driven fjord–coast advection and its potential effect on plankton and fish recruitment. *Fisheries oceanography*, 8(4):255–263.

Aure, J. and Stigebrandt, A. (1989). On the influence of topographic factors upon the oxygen consumption rate in sill basins of fjords. *Estuarine, Coastal and Shelf Science*, 28(1):59–69.

Baines, P. G. (1995). Topographic effects in stratified flows.

Bakketeig, I. E., Hauge, M., and Kvamme, C. (2017). *Havforskningsrapporten 2017*. Fisken og havet.

Berntsen, J. (2004). Users guide for a modesplit σ-coordinate numerical ocean model. *Department of Applied Mathematics, University of Bergen, Tech. Rep*, 135:48.

Berntsen, J., Xing, J., and Davies, A. M. (2008). Numerical studies of internal waves at a sill: Sensitivity to horizontal grid size and subgrid scale closure. *Continental Shelf Research*, 28(10-11):1376–1393.

Blumberg, A. and Mellor, G. (1987). A description of a three-dimensional coastal ocean circulation model, three-dimensional coastal ocean models. *Coastal Estuarine Sci.*, 4.

Cushman-Roisin, B. and Beckers, J. M. (2011). *Introduction to geophysical fluid dynamics: physical and numerical aspects*, volume 101. Academic press.

Haidvogel, D. B. and Beckmann, A. (1999). *Numerical ocean circulation modeling*, volume 2 of *Series on environmental science and management*. Imperial College Press.

Hanert, E., Deleersnijder, E., and Legat, V. (2006). An adaptive finite element water column model using the Mellor-Yamada level 2.5 turbulence closure scheme. *Ocean Modelling*, 12(1-2):205–223.

Institute of Marine Research, I. (2018). Stasjon: Ytre Utsira.

Johansen, P.-O., Isaksen, T. E., Bye-Ingebrigtsen, E., and Cornell, A. S. (2018). Forskeren forteller: Har fjordene på Vestlandet blitt mer sårbare?

Klinck, J. M., O'Brien, J. J., and Svendsen, H. (1981). A simple model of fjord and coastal circulation interaction. *Journal of Physical Oceanography*, 11(12):1612–1626.

Kundu, P. K., Cohen, I. M., and Dowling, D. R. (2016). *Fluid mechanics*. Academic press, sixth edition.

Martinsen, E. A. and Engedahl, H. (1987). Implementation and testing of a lateral boundary scheme as an open boundary condition in a barotropic ocean model. *Coastal engineering*, 11(5-6):603–627.

Mellor, G. L. (1998). *Users guide for a three dimensional, primitive equation, numerical ocean model*. Program in Atmospheric and Oceanic Sciences, Princeton University, NJ.

Mellor, G. L. and Yamada, T. (1982). Development of a turbulence closure model for geophysical fluid problems. *Reviews of Geophysics*, 20(4):851–875.

Sand, R. E. (2018). Water renewal in a threshold fjord: A simulation study of submerged fresh water discharge. Master's thesis, The University of Bergen.

Shapiro, R. (1975). Linear filtering. *Mathematics of Computation*, 29:1094–1097.

Smagorinsky, J. (1963). General circulation experiments with the primitive equations: I. the basic experiment. *Monthly weather review*, 91(3):99–164.

Soltveit, T. and Jensen, P. M. (2018). Bunnvannet i Masfjorden må skiftes ut, mener HI-forskere.

Sætre, R. (2007). *The Norwegian Coastal Current: Oceanography and Climate*. Tapir Academic Press.

Wang, D.-P. (1984). Mutual intrusion of a gravity current and density front formation. *Journal of Physical Oceanography*, 14(7):1191–1199.

Zhang, P., Pang, Y., Pan, H., Shi, C., Huang, Y., and Wang, J. (2015). Factors contributing to hypoxia in the Minjiang river estuary, Southeast China. *International journal of environmental research and public health*, 12(8):9357–9374.